



Full length article

Dynamic wave propagation in micro-torus structures: Implementing a 3D physically realistic theory

I. Karimipour^a, Y. Tadi Beni^{b,c,*}, Hadi Arvin^b, A.H. Akbarzadeh^{d,e}^a Department of Mechanical Engineering, Shahrood University, Shahrood, Iran^b Faculty of Engineering, Shahrood University, Shahrood, Iran^c Nanotechnology Research Center, Shahrood University, Shahrood, Iran^d AM³L Laboratory, Department of Bioresource Engineering, McGill University, Montreal, QC H9X3V9, Canada^e Department of Mechanical Engineering, McGill University, Montreal, QC H3A 0C3, Canada

ARTICLE INFO

Keywords:

Torus structure
Modified couple stress theory
3D elasticity
Helmholtz decomposition technique
Size effect
Laplacian eigenfunctions

ABSTRACT

This paper makes strides to analyze the wave propagation in micro-torus structures with circular cross-sections using the modified couple stress theory (MCST). This physically realistic theory encompasses the material size effect. The fundamental equilibrium equations of MCST in the mathematical framework of toroidal coordinates are first reformulated. Navier's equations resulting from the implementation of MCST for micro-torus structures are treated by employing the Helmholtz decomposition technique. Several micro-torus problems using MCST in the 3D elasticity framework are solved numerically by a finite element method (FEM) to find eigenvalues and eigenfunctions from the elastic wave propagation standpoints. Wave propagation analysis within micro-torus structures and the effects of material length scale parameter on the vibrational response of various geometries, such as a quarter and a half torus along with a cylinder, are investigated. Opposed to the classical continuum theory that fails to describe the dispersion of waves at higher frequencies within micro-torus structures, the MCST can demonstrate the experimentally reported dispersive wave behavior. The findings can be potentially implemented to analyze and design a variety of sensors and actuators as well as medical, telecommunication, and electronic devices. This paper also develops an accurate estimation for the biharmonic and Laplace's toroidal coordinates to study charge distribution in isolated conducting graphene micro-torus structures. Finally, the resulting electrostatic potential and the charge density in a conducting torus surface for electrostatics applications are determined in terms of Legendre functions. Regarding the different cases of arbitrary charge distribution, findings are helpful to control the electronic properties of graphene micro torus and rational design of nano-structures used in nanoscale transistor channels and superconductors. Treating the Laplace equation on a nano torus assists to more precisely realize the high-frequency localization of Laplacian eigenfunctions, i.e., how an eigenfunction is distributed in a small region of the torus domain and decays rapidly outside the region.

1. Introduction

Alternative multifunctional properties of materials, e.g., chemical and electrical reactivity, mechanical strength, optical, magnetic, and electrical characteristics, can be considerably enhanced or altered in micro or nanoscale by considering length scale [1]. The desired multifunctional properties of nanocomposites may be achieved by incorporating nano-sized additives with specific characteristics into a matrix of polymer, ceramic, or metal. Much effort has been directed towards the employment of nanotechnology and nanoscience to design and fabricate engineered nanomaterials with unprecedented functionalities. There is an immense interest in the commercialization of nanomaterials for various applications in energy storage systems, solar and fuel cells, nanoelectronics and semiconductors, optical engineering,

medicines, and drugs. Other nanocomposite applications have been found in exfoliated clay stacks and electrospun (smart) fibers [2,3].

A complete literature review about the studies concerning vibration and buckling analyses of torus structures is addressed in a previous paper by the authors [4]. Fairly thorough literature on this topic and related studies based on the torus structures are summarized here. The dynamic elastic buckling, elastic-plastic buckling, and non-linear vibration of the toroidal shells under different loading conditions have already been examined [5–9]. Free vibrations of toroidal shells, curved pipes, and composite laminated doubly curved shells with various boundary conditions have been thoroughly investigated in the literature [10–14], employing various solutions methodologies, including Rayleigh-Ritz, modified Fourier series, and Chebyshev-Ritz method.

* Corresponding author.

E-mail address: tadi@eng.sku.ac.ir (Y.T. Beni).

Different theories include shell bending, linear elasticity, and first-order shear deformation shell theory, were implemented. Moreover, the Eringen elasticity theory has been employed to elicit the size effects on the mechanical responses of three-dimensional (3D) orthotropic curved nanotubes [10,11].

The elastic waveguide properties of a curved flexible pipe, idealized as a thin-walled toroidal shell, have been investigated [12]. Mechanical vibration propagates along the waveguide in the structures similar to stress and elastic waves. Within the elastic wave propagation field, guided waves (GW) can be present in slender structures, where one or two geometric dimensions are smaller than the others (waveguide) [13]. When an elastic wave approaches a discontinuity, such as crack or locations with abrupt geometrical changes, the elastic waves would be divided into reflected and transmitted waves. In the boundaries of a medium, reflection merely occurs.

The reflection and transmission matrices are derived by applying the continuity and equilibrium conditions of the structure. Combining the relation among propagating, reflecting, and transmitted waves and using the dispersion equation, which presents the relation between wave number and natural frequencies, a straightforward method for finding the natural frequencies is obtained [14]. It should be noticed that the excitation location and the position of the vibration-induced phenomena are not coincident. Thus, the waveguide properties, describing the kind of transmitted wave along with a structure, are a cornerstone for analyzing the behavior of structural elements subjected to dynamic loading and shock waves [12]. The wave-like vibrational response propagates in media at a speed known as the phase speed. The phase speed can be determined in terms of natural frequency and wave number. In the frequency district, several margins have been observed for the system behavior changes. These margins are called cut-off frequencies.

At the micro/nanoscale level, classical elasticity theories, due to the lack of incorporation of the material's internal length scale effects, cease to hold in scientific applications [15]. One of the innate weaknesses of the traditional theory of elasticity is its lack of accuracy in providing the elastic fields of nano-sized inhomogeneities [16]. The size independence of the developed formulations employing methods based on the traditional theory of elasticity is another shortcoming of this theory. To circumvent such dilemmas, various higher-order continuum theories have been developed in the literature. Formulations within such theories involve one or more material length scale parameters linked to the discrete nature of the matter. In the literature, few efforts have been made to calculate the length scale of some solid crystalline materials [17,18]. Incorporating these internal length scale parameters in the formulations improves the classical continuum theory for capturing the size-dependent effects to have a more precise model.

It is therefore essential to determine the internal length scale parameters of nano/microscale materials both computationally and experimentally since they are appeared in the mathematical framework of nonlocal elasticity theory [19], Cosserat's continuum theory [20], strain gradient elasticity theory [21–29], couple stress theory [30–39], and molecular dynamics (MD) simulation results [40–42]. The size effect phenomenon can be associated with the micro/nano-structure of materials from a different viewpoint. The possible source of size effects can emanate from material imperfection, grain or precipitate size, twin boundary spacing or dislocation density, and nano/micro-architecture of the materials [42]. Exhibiting the now-commonly-known phenomenon "extrinsic size effect" shows that the yield strength and the ultimate tensile strength of a single crystal scale with external sample size in a power-law fashion. As both extrinsic (i.e., sample size) and the intrinsic (i.e., microstructural) dimensions play a non-trivial role in the mechanical properties and material deformation mechanisms, it is essential to extend an understanding of their interaction and mutual effects on the material deformation and mechanical properties, especially in micro/nano-structures [43,44].

A critical shortcoming of classical continuum approaches like Es-helby's theory, in addition to their size independence, is their inadequacy in providing an accurate solution in the vicinity of the small defects and inhomogeneities. It is well-known that formulations within the mathematical framework of classical elasticity are restricted to large enough wavelengths and body dimensions compared to the medium of interest [45–47]. Incorporating this notion requires resorting to higher-order continuum theories, which can account for discrete material nature. Based on this thought, strain gradient theories were developed and evolved in the literature. Consideration of the mathematical framework for a strain gradient theory, in general, leads to the introduction of one or more internal length scale parameters, which are inherently accountable for reflecting the discrete nature of the elastic bodies of interest [48–50].

The method of displacement of the toroidal elasticity was established by Redekop [2] (1992). A recent theory allows a broader study of the thick shell, which involves displacement and stress. In 1992, Redekop [2] solved the displacement field in the toroidal shell structure. He expanded 3D equations in circular coordinates. Toroidal Elasticity (TE) theory was used to study stress and displacement in toroidal structures, including rings, elbows, and tubes. Gohner [51] was the first researcher to extend TE theory to scrutinize an isotropic curved solid circular ring sector under pure twist and bending moments. The coordinate system used in Gohner was useful only for the boundary conditions of a solid circular cross-section. In general, TE is classified into two major procedures. Stress-based TE (SBTE) and displacement-based TE (DBTE) have both been used by various researchers to explain the mechanical behavior of curved shells. Stress-Based Toroidal Elasticity (SBTE) was discussed by Lang in 1984 [52]. He performed comprehensive studies, briefed former research [41–43], and developed the SBTE in the toroidal coordinate system under different loadings. He recast the three equilibrium equations and six compatibility equations into the toroidal coordinate system so that the solution satisfied compatibility equations.

In comparison to SBTE, DBTE has the privilege of instantly yielding the displacement fields and stresses. Building on the work of Lang [52], Redekop chose the displacement components as the primary variables and developed the governing Navier's equations in this coordinate system. Redekop [53] considered isotropic curved tubes under in-plane traction by using the DBTE method. The displacement fields and stresses were given up to the third order. The numerical solutions captured for this case were validated with finite element results. Zhu and Redekop [54] introduced a DBTE solution for an isotropic curved tube under the out-of-plane loading condition. They presented the governing Navier's equations up to the third order in a toroidal coordinates system to obtain the displacement components and stress field through an analytical solution. In particular, it is shown that the stress field inside the inclusion is not uniform. This is in contrast with the corresponding results for infinitely-long and finite circular cylindrical bars and spherical balls with cylindrical and spherical inclusions, respectively. Also shown that for a solid torus of any size made of an incompressible linear elastic solid with uniform (infinitesimal) pure dilatational eigenstrains, the stress inside the inclusion is not uniform [55].

In the following recent studies on potential approaches to analyses, microstructures are discussed. Two methods that today are widely used are FEM and Isogeometric Analysis (IGA) [56]. For shell structures that experience large deformation or post-buckling state, it is recommended to use IGA [56] to obtain a good solution with the exact geometry of the shell during loading. This is due to the accumulated geometrical description error of FEM during loading becomes large while that of IGA is completely eliminated using NURBS basic functions. It is well known that the main procedures of FEM and IGA are quite similar. In short, the only difference is the basic being used. This "small" change produces high accuracy for IGA even when curved structures experience large deformation state. Now, it can be concluded that the solutions of FEM and IGA agree well for small and moderate

deformation problems. It is known that Isogeometric Analysis (IGA) arguably outweighs classical finite element method in terms of high continuity and high order differentiability.

Potential approaches to analysis microstructures are also very important to reach accurate results. For instance, a rotation-free isogeometric method with three variables formulated from refined shell theories was proposed in [57]. This novel approach using isogeometric implementation can effectively handle the high order differentiability of the complex geometry and different theory. The numerical results showed the reliability and efficiency of the present method. Also, the NURBS basis functions used in the isogeometric analysis (IGA) are C^{p-1} continuous and can easily satisfy the C^1 continuity condition [58]. It has been shown that the weak form requires only C^1 continuity that can be solved easily by finite element methods based on the Hermite interpolation functions. A new formulation based on arbitrary polytopal composite finite elements was investigated [50] to discretize complicated domains to solve a broad class of mechanics problems. It was shown that the proposed method reaches the theoretical convergence rate and significantly improves the accuracy of polygonal element-based solutions.

A few efforts have been made in the literature to investigate the vibration behavior in confined curved nanotubes using alternative continuum theories, including the Eringen differential model [59–64]. However, no research has focused on the wave propagation in micro-toroidal structures employing non-classical elasticity theories. In what follows, to illustrate the current developments on wave propagation in the micro-torus structures, several examples are studied to demonstrate how the wave propagates on the micro-torus surfaces. To accurately realize how the wave propagates in toroidal structure, 3D elasticity equations are required. As the aim of the current research is to investigate wave propagation in microscale structures, the 3D elasticity equation in the framework of the MCST is derived in the form of Navier's equations. After that, the ensuing relations for Navier's equations are decomposed through the Helmholtz equation into Laplacian and biharmonic ones. For this purpose, for the first time in the open literature, a complete calculation for finding Divergence, Laplacian operator, Laplacian of Laplacian, Gradient, Curl, the divergence of the second-order tensors, the gradient of the divergence for the vector fields, and an arbitrary general scalar function is developed in the toroidal coordinates. Having a Laplacian and a biharmonic equation enables us to find an alternative separation for the Laplace equation in toroidal coordinates, for the electrostatic field as an example. The potential charge outside (inside) a torus and on the torus reference circle, when a uniform line dipole charge density exists around the reference circle inside the torus, is determined.

The fundamental formulations of the MCST in a 3D elastic medium are first reviewed. The MCST governing equations pertinent to 3D elasticity problems in toroidal coordinates are presented. Since the main application of the wave propagation analysis in high-frequency ranges is in damage detection and cut-off frequencies, the findings and the methodology presented in this study can be exploited to analyze the damaged torus structures to detect the damage location. The wave propagation characteristics in the torus structures demonstrate how the elastic waves are affected by the micro-tours curvature.

2. Equation of motion in terms of Navier's equation

The vector analysis in the toroidal coordinates is developed according to the scale factors for the first time. Then, employing the scale factors, the vector operators are calculated in the toroidal coordinates. Finally, the motion equations for the toroidal bodies are obtained through Navier's equation alongside the frequency equations by applying the boundary conditions. Toroidal coordinates can be considered as a result of rotating the two-dimensional (2D) bipolar coordinate system [65]:

$$Z = ia \coth \frac{1}{2}\zeta, \quad \zeta = \tau + i\sigma \quad (1)$$

where a is a constant that gives the radius of a circumference in the $Z = 0$ plane described by $\tau \rightarrow \infty$ (that is when $\tau \rightarrow \infty$ we have $X = a \cos \phi$, $Y = a \sin \phi$, and $Z = 0$). τ and σ are the curvilinear coordinates about the axis that separates its two focal points, and Z is a complex number. Thus, the two focal points in bipolar coordinates create a ring of radius a in the XY plane of the toroidal coordinate system, while the Z -axis is the rotation axis (see Fig. 1). Tori formed from the rotation of a circle on the X -axis with a circular cross-section with a radius of $\frac{a}{\sinh(\tau)}$. It should be noted that in the case of a complete toroidal shell in the circumferential direction (ϕ), considering the axial symmetry condition around the Z -axis (Fig. 1), the displacement field would consist of two radial and meridional displacement components. The distance between the Z -axis and the center of each circle is $a \coth(\tau)$, which means that in this toroidal coordinate, the following relation is established $4a^2(X^2 + Y^2)\coth^2(\tau) - (X^2 + Y^2 + Z^2 + a^2)^2 = 0$. The focal ring is also called the reference circle [67]. Solving Eq. (1) in terms of the parameter ζ leads to $\zeta = \text{Log} \frac{Z+ia}{Z-ia} = \text{Log} \frac{\tau_1 e^{i\sigma_1}}{\tau_2 e^{i\sigma_2}}$. By implementing polar relations, this relation is converted into $\tau + i\sigma = \text{Log} \frac{\tau_1}{\tau_2} + i(\sigma_1 - \sigma_2)$. The coordinate ranges are $-\pi < \sigma \leq \pi$, $\tau \geq 0$, and $0 < \phi < 2\pi$. The most popular definition of the toroidal coordinates (σ, τ, ϕ) is

$$X = \frac{a \sinh(\tau) \cos \phi}{\cosh(\tau) - \cos \sigma}, \quad Y = \frac{a \sinh(\tau) \sin \phi}{\cosh(\tau) - \cos \sigma}, \quad \text{and} \quad Z = \frac{a \sin \sigma}{\cosh(\tau) - \cos \sigma} \quad (2)$$

The inverse transformations are given by:

$$\begin{aligned} \tau &= \arctan h \frac{2a\sqrt{X^2 + Y^2}}{X^2 + Y^2 + Z^2 + a^2}, \quad \sigma = \arctan \frac{2Za}{X^2 + Y^2 + Z^2 - a^2}, \quad \text{and} \\ \phi &= \arctan \frac{Y}{X}. \end{aligned} \quad (3)$$

There is no universally agreed-upon definition; thus, the use of symbols and the order of the coordinates differs among the references. Scale factors are calculated as follows:

$$h_{\sigma=1} = h_{\tau=2} \frac{a}{\cosh(\tau) - \cos \sigma}, \quad h_{\phi=3} = \frac{a \sinh(\tau)}{\cosh(\tau) - \cos \sigma} \quad (4)$$

The use of scale factors allows the Jacobian matrix to be calculated as follows:

$$\begin{aligned} J &= \begin{bmatrix} \frac{1}{h_\sigma} \frac{\partial X}{\partial \sigma} & \frac{1}{h_\sigma} \frac{\partial Y}{\partial \sigma} & \frac{1}{h_\sigma} \frac{\partial Z}{\partial \sigma} \\ \frac{1}{h_\tau} \frac{\partial X}{\partial \tau} & \frac{1}{h_\tau} \frac{\partial Y}{\partial \tau} & \frac{1}{h_\tau} \frac{\partial Z}{\partial \tau} \\ \frac{1}{h_\phi} \frac{\partial X}{\partial \phi} & \frac{1}{h_\phi} \frac{\partial Y}{\partial \phi} & \frac{1}{h_\phi} \frac{\partial Z}{\partial \phi} \end{bmatrix} \\ &= \begin{bmatrix} -\sin \sigma \sinh(\tau) \cos \phi & -\sin \sigma \sinh(\tau) \sin \phi & \cosh(\tau) \cos \sigma - 1 \\ \cosh(\tau) - \cos \sigma & \cosh(\tau) - \cos \sigma & \cosh(\tau) - \cos \sigma \\ \cos \phi(1 - \cosh(\tau) \cos \sigma) & \sin \phi(1 - \cosh(\tau) \cos \sigma) & -\sin \sigma \sinh(\tau) \\ \cosh(\tau) - \cos \sigma & \cosh(\tau) - \cos \sigma & \cosh(\tau) - \cos \sigma \\ -\sin \phi & \cos \phi & 0 \end{bmatrix} \end{aligned} \quad (5)$$

The Jacobian matrix (J) determinant defines a ratio of the volumetric changes between the Cartesian and the toroidal coordinates. The gradient of a general scalar function in the toroidal coordinate can be stated as follows:

$$\bar{\nabla} f = \frac{(\cosh(\tau) - \cos(\sigma))}{a} \left(\frac{\partial f}{\partial \sigma} \bar{\mathbf{e}}_\sigma + \frac{\partial f}{\partial \tau} \bar{\mathbf{e}}_\tau + \frac{1}{\sinh(\tau)} \frac{\partial f}{\partial \phi} \bar{\mathbf{e}}_\phi \right) \quad (6)$$

in which an overbar denotes the unit vectors. Accordingly, the divergence of a vector \mathbf{u} in the toroidal coordinate read:

$$\begin{aligned} \bar{\nabla} \cdot \mathbf{u} &= \frac{\cosh(\tau) - \cos(\sigma)}{a} \frac{\partial u_\sigma}{\partial \sigma} + \frac{(\cosh(\tau) - \cos(\sigma))}{a} \frac{\partial u_\tau}{\partial \tau} \\ &\quad + \frac{2 - \cosh(\tau)(\cosh(\tau) + \cos(\sigma))}{a \sinh(\tau)} u_\tau \\ &\quad - \frac{2}{a} u_\sigma \sin(\sigma) + \frac{\partial u_\phi}{\partial \phi} \frac{(\cosh(\tau) - \cos(\sigma))}{a \sinh(\tau)} \end{aligned} \quad (7)$$

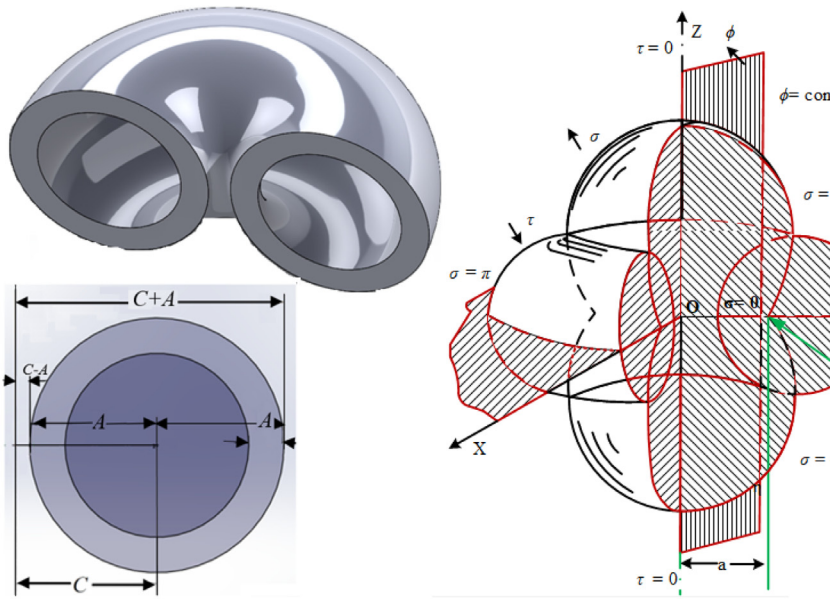


Fig. 1. Illustration of a partial torus structure [66].

Moreover, the Laplacian operator for an arbitrary general scalar function, i.e., the divergence of the gradient of a general function in the toroidal coordinate, is determined through:

$$\begin{aligned} \bar{\nabla}^2 u = \bar{\nabla} \cdot (\bar{\nabla} u) &= -\frac{\cosh(\tau) - \cos(\sigma)}{a^2 (\sinh(\tau))^2} \left(-(\cosh(\tau) - \cos(\sigma)) \right. \\ &\quad \left[\left(\frac{\partial^2 u}{\partial \sigma^2} + \frac{\partial^2 u}{\partial \tau^2} \right) (\sinh(\tau))^2 \right. \\ &\quad \left. + \frac{\partial^2 u}{\partial \phi^2} \right] + ((\sinh(\tau))^2 \sin(\sigma)) \frac{\partial u}{\partial \sigma} + \sinh(\tau) (\cosh(\tau) \cos(\sigma) - 1) \frac{\partial u}{\partial \tau} \end{aligned} \quad (8)$$

The gradient $\bar{\nabla} = \frac{1}{h_i} \frac{\partial}{\partial \xi^i} \bar{\mathbf{e}}_i$, $i = (\underbrace{\sigma}_1, \underbrace{\tau}_2, \underbrace{\phi}_3)$, i.e., $\bar{\nabla} u \equiv \bar{T} =$

$\frac{\partial(u_n \bar{\mathbf{e}}_n)}{h_m \partial \xi^m}$ of a general vector field $\mathbf{u} = u_n \bar{\mathbf{e}}_n$ (results into a second-order tensor) in the curvilinear coordinate system and the toroidal coordinate system, is exhibited in Eqs. (9) given in Box I and (10), where the notations $(-)$ and $(\underline{})$ show that \mathbf{e} and T are first and second-order tensors, respectively.

$$\begin{aligned} T_{\sigma\sigma} &= \left(\frac{\cosh \tau - \cos \sigma}{a} \right) \frac{\partial \mathbf{u}_\sigma}{\partial \sigma} - \frac{\sinh \tau}{a} \mathbf{u}_\tau, \\ T_{\sigma\tau} &= \frac{\sinh \tau}{a} \mathbf{u}_\sigma + \left(\frac{\cosh \tau - \cos \sigma}{a} \right) \frac{\partial \mathbf{u}_\tau}{\partial \sigma}, \\ T_{\sigma\phi} &= \left(\frac{\cosh \tau - \cos \sigma}{a} \right) \frac{\partial \mathbf{u}_\phi}{\partial \sigma}, \quad T_{\tau\sigma} = \left(\frac{\cosh \tau - \cos \sigma}{a} \right) \frac{\partial \mathbf{u}_\sigma}{\partial \tau} + \frac{\sin \sigma}{a} \mathbf{u}_\tau, \\ T_{\tau\tau} &= \left(\frac{\cosh \tau - \cos \sigma}{a} \right) \frac{\partial \mathbf{u}_\tau}{\partial \tau} - \frac{\sin \sigma}{a} \mathbf{u}_\sigma, \quad T_{\tau\phi} = \left(\frac{\cosh \tau - \cos \sigma}{a} \right) \frac{\partial \mathbf{u}_\phi}{\partial \tau}, \\ T_{\phi\sigma} &= \left(\frac{\cosh \tau - \cos \sigma}{a \sinh \tau} \right) \frac{\partial \mathbf{u}_\sigma}{\partial \phi} + \frac{\sin \sigma}{a} \mathbf{u}_\phi, \quad T_{\phi\tau} = \left(\frac{\cosh \tau - \cos \sigma}{a \sinh \tau} \right) \frac{\partial \mathbf{u}_\tau}{\partial \phi} \\ &\quad - \left(\frac{1 - \cosh \tau \cos \sigma}{a \sinh \tau} \right) \mathbf{u}_\phi, \\ T_{\phi\phi} &= -\frac{\sin \sigma}{a} \mathbf{u}_\sigma + \left(\frac{1 - \cosh \tau \cos \sigma}{a \sinh \tau} \right) \mathbf{u}_\tau + \left(\frac{\cosh \tau - \cos \sigma}{a \sinh \tau} \right) \frac{\partial \mathbf{u}_\phi}{\partial \phi} \end{aligned} \quad (10)$$

Furthermore, the Laplacian of Laplacian for an arbitrary general scalar function in the toroidal coordinates, i.e., $\bar{\nabla}^4 u$, is defined by:

$$\begin{aligned} \bar{\nabla}^4 u &= \frac{1}{a^4 (\sinh(\tau))^4} \left(\left(\left(\frac{\partial^4 u}{\partial \sigma^4} + \frac{2 \partial^4 u}{\partial \tau^2 \partial \sigma^2} + \frac{\partial^4 u}{\partial \tau^4} \right) (\sinh(\tau))^4 \right. \right. \\ &\quad \left. \left. + \left(\frac{2 \partial^4 u}{\partial \sigma^2 \partial \phi^2} + \frac{2 \partial^4 u}{\partial \tau^2 \partial \phi^2} \right) \right. \right. \\ &\quad \left. \left. (\sinh(\tau))^2 + \frac{\partial^4 u}{\partial \phi^4} + \frac{4 \partial^2 u}{\partial \phi^2} \right) (\cosh(\tau) - \cos(\sigma))^4 \right) \end{aligned}$$

$$\begin{aligned} &+ \left(\left(\frac{2 \partial^3 u}{\partial \sigma^3} + \frac{2 \partial^3 u}{\partial \tau^2 \partial \sigma} \right) (\sinh(\tau))^4 \sin(\sigma) \right. \\ &\quad + 2 (2 (\cosh(\tau))^2 - \cosh(\tau) \cos(\sigma) - 1) \left(\frac{\partial^3 u}{\partial \tau^3} + \frac{\partial^3 u}{\partial \tau \partial \sigma^2} \right) (\sinh(\tau))^3 \\ &\quad + 2 \frac{\partial^3 u}{\partial \tau \partial \phi^2} \\ &\quad (\cosh(\tau) \cos(\sigma) - 1) \sinh(\tau) (\cosh(\tau) - \cos(\sigma))^3 \\ &\quad + \left((-2 (\sinh(\tau))^4 \cos(\sigma) \frac{\partial u}{\partial \sigma} - 2 (\cosh(\tau) \cos(\sigma) - 1) \frac{\partial^2 u}{\partial \tau \partial \sigma} (\sinh(\tau))^3 \right. \\ &\quad + 2 \frac{\partial^3 u}{\partial \sigma \partial \phi^2} (\cosh(\tau) - \cos(\sigma)) (\sinh(\tau))^2 \left. \right) \sin(\sigma) + \frac{\partial^2 u}{\partial \sigma^2} \\ &\quad (4 (\cosh(\tau))^2 - 4 \cosh(\tau) \cos(\sigma) + (\cos(\sigma))^2 - 1) (\sinh(\tau))^4 \\ &\quad + (-1 + 4 (\cosh(\tau))^4 - 4 \cos(\sigma) (\cosh(\tau))^3 + (-(\cos(\sigma))^2 - 4) (\cosh(\tau))^2 \\ &\quad + 6 \cosh(\tau) \cos(\sigma) \frac{\partial^2 u}{\partial \tau^2} (\sinh(\tau))^2 - 2 \frac{\partial u}{\partial \tau} \left(\left((\cosh(\tau))^3 - \frac{3 \cosh(\tau)}{2} \right) \right. \\ &\quad \left. (\cos(\sigma))^2 + \cos(\sigma) - \frac{(\cosh(\tau))^3}{2} \right) \sinh(\tau) \right) (\cosh(\tau) - \cos(\sigma))^2 \end{aligned} \quad (11)$$

Moreover, the curl of a vector \mathbf{u} in the toroidal coordinate is calculated as below:

$$\begin{aligned} \bar{\nabla} \times \mathbf{u} &= \left(\frac{-(\cosh(\tau) - \cos(\sigma))}{a (\sinh(\tau))} \frac{\partial \mathbf{u}_\tau}{\partial \phi} + \frac{(\cosh(\tau) - \cos(\sigma))}{a} \frac{\partial \mathbf{u}_\phi}{\partial \tau} \right. \\ &\quad \left. - \frac{(\cosh(\tau) \cos(\sigma) - 1)}{a (\sinh(\tau))} \mathbf{u}_\phi \right) \bar{\mathbf{e}}_\sigma \\ &\quad + \left(\frac{(\cosh(\tau) - \cos(\sigma))}{a (\sinh(\tau))} \frac{\partial \mathbf{u}_\sigma}{\partial \phi} - \frac{(\cosh(\tau) - \cos(\sigma)) \frac{\partial \mathbf{u}_\phi}{\partial \sigma} - \sin(\sigma) \mathbf{u}_\phi}{a} \right) \bar{\mathbf{e}}_\tau \\ &\quad + \frac{(\cosh(\tau) - \cos(\sigma)) \left(\frac{\partial \mathbf{u}_\tau}{\partial \sigma} - \frac{\partial \mathbf{u}_\sigma}{\partial \tau} \right) + \mathbf{u}_\sigma \sinh(\tau) - \mathbf{u}_\tau \sin(\sigma)}{a} \bar{\mathbf{e}}_\phi \end{aligned} \quad (12)$$

On the other hand, the divergence of the second-order tensor $(\bar{T} = T_{mn} \bar{\mathbf{e}}_m \bar{\mathbf{e}}_n)$, which is a first-order tensor (vector), i.e., $\bar{\nabla} \cdot \bar{T} = (\bar{\mathbf{e}}_r \frac{1}{h_r} \frac{\partial}{\partial \xi^r}) \cdot (T_{mn} \bar{\mathbf{e}}_m \bar{\mathbf{e}}_n)$, read:

$$\begin{aligned} \bar{\nabla} \cdot \bar{T} &= \frac{1}{h_1 h_2 h_3} \left[\frac{\partial}{\partial \xi^1} (T_{11} h_2 h_3) + \frac{\partial}{\partial \xi^2} (T_{21} h_1 h_3) \right. \\ &\quad \left. + \frac{\partial}{\partial \xi^3} (T_{31} h_1 h_2) + h_2 T_{13} \frac{\partial h_1}{\partial \xi^3} + h_3 T_{12} \frac{\partial h_1}{\partial \xi^2} \right] \end{aligned}$$

$$\underline{\underline{T}} = \begin{bmatrix} \frac{1}{h_1} \frac{\partial \mathbf{u}_1}{\partial \xi^1} + \frac{\mathbf{u}_2}{h_1 h_2} \frac{\partial h_1}{\partial \xi^2} + \frac{\mathbf{u}_3}{h_1 h_3} \frac{\partial h_1}{\partial \xi^3} & \frac{-\mathbf{u}_1}{h_1 h_2} \frac{\partial h_1}{\partial \xi^2} + \frac{1}{h_1} \frac{\partial \mathbf{u}_2}{\partial \xi^1} & -\frac{\mathbf{u}_1}{h_1 h_3} \frac{\partial h_1}{\partial \xi^3} + \frac{1}{h_1} \frac{\partial \mathbf{u}_3}{\partial \xi^1} \\ \frac{1}{h_2} \frac{\partial \mathbf{u}_1}{\partial \xi^2} - \frac{\mathbf{u}_2}{h_1 h_2} \frac{\partial h_2}{\partial \xi^1} & \frac{1}{h_2} \frac{\partial \mathbf{u}_2}{\partial \xi^2} + \frac{\mathbf{u}_3}{h_2 h_3} \frac{\partial h_2}{\partial \xi^3} + \frac{\mathbf{u}_1}{h_1 h_2} \frac{\partial h_2}{\partial \xi^1} & -\frac{\mathbf{u}_2}{h_2 h_3} \frac{\partial h_2}{\partial \xi^3} + \frac{1}{h_2} \frac{\partial \mathbf{u}_3}{\partial \xi^2} \\ \frac{1}{h_3} \frac{\partial \mathbf{u}_1}{\partial \xi^3} - \frac{\mathbf{u}_3}{h_1 h_3} \frac{\partial h_3}{\partial \xi^1} & \frac{1}{h_3} \frac{\partial \mathbf{u}_2}{\partial \xi^3} - \frac{\mathbf{u}_3}{h_2 h_3} \frac{\partial h_3}{\partial \xi^2} & \frac{\mathbf{u}_1}{h_1 h_3} \frac{\partial h_3}{\partial \xi^1} + \frac{\mathbf{u}_2}{h_2 h_3} \frac{\partial h_3}{\partial \xi^2} + \frac{1}{h_3} \frac{\partial \mathbf{u}_3}{\partial \xi^3} \end{bmatrix} \quad (9)$$

Box I.

$$\begin{aligned} & -T_{22} h_3 \frac{\partial h_2}{\partial \xi^1} - h_2 T_{33} \frac{\partial h_3}{\partial \xi^1} \Big] \bar{\mathbf{e}}_1 + \frac{1}{h_1 h_2 h_3} \left[\frac{\partial}{\partial \xi^1} (T_{12} h_2 h_3) \right. \\ & + \frac{\partial}{\partial \xi^2} (T_{22} h_1 h_3) + \frac{\partial}{\partial \xi^3} (T_{32} h_1 h_2) \\ & + h_3 T_{21} \frac{\partial h_2}{\partial \xi^1} - h_3 T_{11} \frac{\partial h_1}{\partial \xi^2} - h_1 T_{33} \frac{\partial h_3}{\partial \xi^2} + h_1 T_{22} \frac{\partial h_2}{\partial \xi^3} \Big] \bar{\mathbf{e}}_2 \\ & + \frac{1}{h_1 h_2 h_3} \left[\frac{\partial}{\partial \xi^1} (T_{13} h_2 h_3) \right. \\ & + \frac{\partial}{\partial \xi^2} (T_{23} h_1 h_3) + \frac{\partial}{\partial \xi^3} (T_{33} h_1 h_2) + h_2 T_{31} \frac{\partial h_3}{\partial \xi^1} + T_{32} h_1 \frac{\partial h_3}{\partial \xi^2} \\ & \left. - h_2 T_{11} \frac{\partial h_1}{\partial \xi^3} - h_1 T_{22} \frac{\partial h_2}{\partial \xi^2} \right] \bar{\mathbf{e}}_3 \end{aligned} \quad (13)$$

Using Eq. (4), the divergence of a second-order tensor in the toroidal coordinates is demonstrated in Eq. (14) in the component form of $\bar{\nabla} \cdot \underline{\underline{T}} = (\bar{\nabla} \cdot \underline{\underline{T}})_\sigma \bar{\mathbf{e}}_\sigma + (\bar{\nabla} \cdot \underline{\underline{T}})_\tau \bar{\mathbf{e}}_\tau + (\bar{\nabla} \cdot \underline{\underline{T}})_\phi \bar{\mathbf{e}}_\phi$:

$$\begin{aligned} (\bar{\nabla} \cdot \underline{\underline{T}})_\sigma &= \left(\frac{\cosh \tau - \cos \sigma}{a} \right)^2 \frac{\partial^2 \mathbf{u}_\sigma}{\partial \sigma^2} - \left(\frac{\cosh \tau - \cos \sigma}{a^2} \right) \sin \sigma \frac{\partial \mathbf{u}_\sigma}{\partial \sigma} \\ &- \frac{2(\cosh \tau - \cos \sigma) \sinh \tau}{a^2} \frac{\partial \mathbf{u}_\tau}{\partial \sigma} \\ &+ \frac{\sin \sigma (\sinh^2 \tau + 2 - 2 \cosh \tau \cos \sigma)}{a^2 \sinh \tau} \mathbf{u}_\tau - \frac{(2 \sin^2 \sigma + \sinh^2 \tau)}{a^2} \mathbf{u}_\sigma \\ &+ \frac{2 \sin \sigma (\cosh \tau - \cos \sigma)}{a^2} \frac{\partial \mathbf{u}_\tau}{\partial \tau} \\ &+ \frac{(\cosh \tau - \cos \sigma)(1 - \cosh \tau \cos \sigma)}{a^2 \sinh \tau} \frac{\partial \mathbf{u}_\sigma}{\partial \tau} + \left(\frac{\cosh \tau - \cos \sigma}{a} \right)^2 \frac{\partial^2 \mathbf{u}_\sigma}{\partial \tau^2} \\ &+ \left(\frac{\cosh \tau - \cos \sigma}{a \sinh \tau} \right)^2 \frac{\partial^2 \mathbf{u}_\sigma}{\partial \phi^2} \\ &+ \frac{2(\cosh \tau - \cos \sigma) \sin \sigma}{a^2 \sinh \tau} \frac{\partial \mathbf{u}_\phi}{\partial \phi}, \\ (\bar{\nabla} \cdot \underline{\underline{T}})_\tau &= \frac{2 \sin \text{ht} (\cosh \tau - \cos \sigma)}{a^2} \frac{\partial \mathbf{u}_\sigma}{\partial \sigma} - \frac{\sin \sigma (\cosh \tau - \cos \sigma)}{a^2} \frac{\partial \mathbf{u}_\tau}{\partial \sigma} \\ &+ \left(\frac{\cosh \tau - \cos \sigma}{a} \right)^2 \frac{\partial^2 \mathbf{u}_\tau}{\partial \sigma^2} \\ &+ \frac{(1 - \cosh \tau \cos \sigma)(\cosh \tau - \cos \sigma)}{a^2 \sinh \tau} \frac{\partial \mathbf{u}_\tau}{\partial \tau} + \left(\frac{\cosh \tau - \cos \sigma}{a} \right)^2 \frac{\partial^2 \mathbf{u}_\tau}{\partial \tau^2} \\ &- \frac{2 \sin \sigma (\cosh \tau - \cos \sigma)}{a^2} \frac{\partial \mathbf{u}_\sigma}{\partial \tau} \\ &+ \left(\frac{\cosh \tau - \cos \sigma}{a \sinh \tau} \right)^2 \frac{\partial^2 \mathbf{u}_\tau}{\partial \phi^2} - \frac{2(1 - \cosh \tau \cos \sigma)(\cosh \tau - \cos \sigma)}{a^2 \sinh^2 \tau} \frac{\partial \mathbf{u}_\phi}{\partial \phi} \\ &- \frac{\sin \sigma \sinh \tau}{a^2} \mathbf{u}_\sigma \\ &+ \frac{\sin^2 \sigma - 2(1 - \cosh \tau \cos \sigma) - \sinh^2 \tau \cosh^2 \tau}{a^2 \sinh^2 \tau} \mathbf{u}_\tau, \\ (\bar{\nabla} \cdot \underline{\underline{T}})_\phi &= \left(\frac{\cosh \tau - \cos \sigma}{a} \right)^2 \frac{\partial^2 \mathbf{u}_\phi}{\partial \sigma^2} - \frac{\sin \sigma (\cosh \tau - \cos \sigma)}{a^2} \frac{\partial \mathbf{u}_\phi}{\partial \sigma} \\ &+ \left(\frac{\cosh \tau - \cos \sigma}{a} \right)^2 \frac{\partial^2 \mathbf{u}_\phi}{\partial \tau^2} \\ &+ \frac{(1 - \cosh \tau \cos \sigma)(\cosh \tau - \cos \sigma)}{a^2 \sinh \tau} \frac{\partial \mathbf{u}_\phi}{\partial \tau} - \frac{2 \sin \sigma (\cosh \tau - \cos \sigma)}{a^2 \sinh \tau} \frac{\partial \mathbf{u}_\sigma}{\partial \phi} \\ &+ \frac{2(1 - \cosh \tau \cos \sigma)(\cosh \tau - \cos \sigma)}{a^2 \sinh^2 \tau} \frac{\partial \mathbf{u}_\tau}{\partial \phi} - \left(\frac{\cosh \tau - \cos \sigma}{a \sinh \tau} \right)^2 \mathbf{u}_\phi \\ &+ \left(\frac{\cosh \tau - \cos \sigma}{a \sinh \tau} \right)^2 \frac{\partial^2 \mathbf{u}_\phi}{\partial \phi^2} \end{aligned} \quad (14)$$

The Laplacian of Laplacian \mathbf{u} in the toroidal coordinates, i.e. $\bar{\nabla}^2 (\bar{\nabla}^2 \mathbf{u}) = \bar{\nabla}^4 \mathbf{u}$, can be determined in the same way; however, for the sake of brevity, it is presented in Supplementary Materials (A).

Furthermore, the gradient of the divergence vector field $\mathbf{u}_\sigma (\sigma, \tau, \phi)$, $\mathbf{u}_\tau (\sigma, \tau, \phi)$, and $\mathbf{u}_\phi (\sigma, \tau, \phi)$ is determined by:

$$\begin{aligned} \bar{\nabla} (\bar{\nabla} \cdot \mathbf{u}) &= \left[\frac{1}{\sinh(\tau) a^2} \left(\left(\left(\frac{\partial^2 \mathbf{u}_\sigma}{\partial \sigma^2} + \frac{\partial^2 \mathbf{u}_\tau}{\partial \tau \partial \sigma} \right) \sinh(\tau) + \frac{\partial^2 \mathbf{u}_\phi}{\partial \sigma \partial \phi} \right) \right. \right. \\ &(\cosh(\tau) - \cos(\sigma))^2 + \left(\left(\frac{\partial \mathbf{u}_\tau}{\partial \tau} - \frac{\partial \mathbf{u}_\sigma}{\partial \sigma} \right) \right. \\ &\sinh(\tau) + \cosh(\tau) \mathbf{u}_\tau + \frac{\partial \mathbf{u}_\phi}{\partial \phi} \left. \right) \sin(\sigma) - 2 \mathbf{u}_\sigma \sinh(\tau) \cos(\sigma) \\ &- \frac{\partial \mathbf{u}_\tau}{\partial \sigma} (\cosh(\tau)^2 + \cosh(\tau) \cos(\sigma) - 2) \left. \right) \\ &\left. \left. \left(\cosh(\tau) - \cos(\sigma) \right) \right] \bar{\mathbf{e}}_\sigma + \left[\frac{1}{\sinh(\tau)^2 a^2} \left(\frac{\sinh(\tau) \partial^2 \mathbf{u}_\phi}{\partial \tau \partial \phi} (\cosh(\tau) - \cos(\sigma))^2 \right. \right. \\ &+ ((-2 \cosh(\tau)^2 + 2)) \\ &\frac{\partial \mathbf{u}_\sigma}{\partial \tau} \sin(\sigma) + \left(\cosh(\tau)^2 \frac{\partial \mathbf{u}_\sigma}{\partial \sigma} - \cosh(\tau) \cos(\sigma) \frac{\partial \mathbf{u}_\tau}{\partial \tau} - \frac{\partial \mathbf{u}_\sigma}{\partial \sigma} + \frac{\partial \mathbf{u}_\tau}{\partial \tau} \right) \sinh(\tau) \\ &+ \sinh(\tau)^2 (\cosh(\tau) - \cos(\sigma)) \\ &\frac{\partial^2 \mathbf{u}_\sigma}{\partial \tau \partial \sigma} + ((\sinh(\tau))^2 (\cosh(\tau) - \cos(\sigma))) \frac{\partial^2 \mathbf{u}_\tau}{\partial \tau^2} + (\cosh(\tau) \cos(\sigma) - 1) \frac{\partial \mathbf{u}_\phi}{\partial \phi} \\ &- \mathbf{u}_\tau ((\cosh(\tau))^3 - \cos(\sigma))) \\ &\left. \left. \left(\cosh(\tau) - \cos(\sigma) \right) \right] \bar{\mathbf{e}}_\tau + \left[\frac{1}{(\sinh(\tau))^2 a^2} \left(\left(\left(\frac{\partial^2 \mathbf{u}_\sigma}{\partial \sigma \partial \phi} + \frac{\partial^2 \mathbf{u}_\tau}{\partial \tau \partial \phi} \right) \sinh(\tau) \right. \right. \right. \right. \\ &+ \frac{\partial^2 \mathbf{u}_\phi}{\partial \phi^2} \left. \right) (\cosh(\tau) - \cos(\sigma))^2 \\ &+ \left(-2 \sinh(\tau) \left(\frac{\partial \mathbf{u}_\sigma}{\partial \phi} \right) \sin(\sigma) - ((\cosh(\tau))^2 + \cosh(\tau) \cos(\sigma) - 2) \frac{\partial \mathbf{u}_\tau}{\partial \phi} \right) \\ &\times (\cosh(\tau) - \cos(\sigma)) \left. \right) \left. \bar{\mathbf{e}}_\phi \right] \end{aligned} \quad (15)$$

3. Constitutive relations in classical and modified couple stress theories

This monograph aims to provide a simple, complete, and systematic presentation of the 3D formulation of micro torus structures in the framework of MCST. In this section, constitutive relations in the framework of the classical theory and the MCST are introduced. It should be noted that the formulation considered in this research is based on the 3D elasticity in the framework of the MCST.

3.1. Classical continuum theory

The strain and stress fields are related to each other as follows [4, 68]

$$t_{ij} = \lambda \epsilon_{ij} \delta_{ij} + 2 \mu \epsilon_{ij}, \quad (16)$$

where t_{ij} and ϵ_{ij} ($i, j = \sigma, \tau, \phi$) are the stress and strain tensors components, respectively, while σ, τ, ϕ are the torus coordinates. Moreover,

$\lambda = \frac{Ev}{(1+v)(1-2v)}$ and $\mu = \frac{E}{2(1+v)}$ are Lamé's constants (μ known as shear modulus) are related to the modulus of elasticity E and the Poisson's ratio v .

3.2. Modified couple stress theory

According to the MCST assumptions, both strain and curvature tensors contribute to the strain energy density [69]. Comparing to the classical continuum mechanics theory, the modified couple stress theory has one high-order parameter (called material length scale parameter) more than the two classical Lamé's constants in its constitutive relations for elastic isotropic materials. Accordingly, the couple stress tensor and the curvature tensor relation read [70]:

$$m_{ij} = 2\mu l^2 \chi_{ij}, \quad (17)$$

where l is a material length scale parameter, which can be estimated through special experimental tests. m_{ij} and χ_{ij} are the deviatoric part of the couple stress tensor and the symmetric curvature tensor, respectively, the latter is defined by [70]:

$$\chi_{ij} = \frac{1}{2}(\nabla\Theta + \nabla\Theta^T) = \frac{1}{2}(\Theta_{i,j} + \Theta_{j,i}) \quad (18)$$

where Θ_i is the rotation vector. The non-zero components of this vector are defined as $\bar{\Theta} = \frac{1}{2}\operatorname{curl}(\bar{u})$.

3.3. Stresses tensor in the toroidal coordinates

The gradient of the displacement vector is calculated according to Eq. (9). The half summation of this tensor and its transpose delivers the strain tensor, i.e., $\epsilon = \frac{1}{2}(\nabla u + u\nabla)$:

$$\begin{aligned} \epsilon_{\sigma\sigma} &= \sqrt{J_2} \frac{\partial u_\sigma}{\partial \sigma} - \frac{J_{13}}{a} u_\tau, \quad \epsilon_{\sigma\tau} = \epsilon_{\tau\sigma} = \frac{\sqrt{J_2}}{2} \frac{\partial u_\tau}{\partial \sigma} + \frac{J_{13}}{2a} u_\sigma \\ &+ \frac{\sqrt{J_2}}{2} \frac{\partial u_\sigma}{\partial \tau} + \frac{J_{12}}{2a} u_\tau, \\ \epsilon_{\sigma\phi} = \epsilon_{\phi\sigma} &= \frac{\sqrt{J_2}}{2} \frac{\partial u_\phi}{\partial \sigma} + \frac{\sqrt{J_2 J_3}}{2} \frac{\partial u_\sigma}{\partial \phi} + \frac{J_{12}}{2a} u_\phi, \quad \epsilon_{\tau\tau} = \sqrt{J_2} \frac{\partial u_\tau}{\partial \tau} - \frac{J_{12}}{a} u_\sigma, \\ \epsilon_{\tau\phi} = \epsilon_{\phi\tau} &= \frac{1}{2} \sqrt{J_2} \frac{\partial u_\phi}{\partial \tau} + \frac{\sqrt{J_2 J_3}}{2} \frac{\partial u_\tau}{\partial \phi} + \frac{1}{2} \left(\frac{J_{22}}{a J_{13}} \right) u_\phi, \\ \epsilon_{\phi\phi} &= \sqrt{J_2 J_3} \frac{\partial u_\phi}{\partial \phi} - \frac{J_{12}}{a} u_\sigma - \left(\frac{J_{22}}{a J_{13}} \right) u_\tau, \end{aligned} \quad (19)$$

From Eq. (19), it can be found that the strain tensor is symmetric. On the other hand, the symmetric curvature tensors, which are employed in the MCST formulation, is computed employing Eq. (18):

$$\begin{aligned} \chi_{\sigma\sigma} &= \frac{\sqrt{J_2}}{2} \frac{\partial}{\partial \sigma} \left(-\sqrt{J_3 J_2} \frac{\partial u_\tau}{\partial \phi} + \sqrt{J_2} \frac{\partial u_\phi}{\partial \tau} - \frac{J_{22}}{a J_{13}} u_\phi \right) \\ &- \frac{J_{13}}{2a} \left(\sqrt{J_3 J_2} \frac{\partial u_\sigma}{\partial \phi} - \sqrt{J_2} \frac{\partial u_\phi}{\partial \sigma} + \frac{J_{12} u_\phi}{a} \right), \quad \chi_{\sigma\tau} \\ &= \chi_{\tau\sigma} = \frac{J_{13}}{4a} \left(-\sqrt{J_3 J_2} \frac{\partial u_\tau}{\partial \phi} + \sqrt{J_2} \frac{\partial u_\phi}{\partial \tau} - \frac{J_{22}}{a J_{13}} u_\phi \right) \\ &+ \frac{\sqrt{J_2}}{4} \frac{\partial}{\partial \sigma} \left(\sqrt{J_3 J_2} \frac{\partial u_\sigma}{\partial \phi} - \sqrt{J_2} + \frac{J_{12} u_\phi}{a} \right) \\ &+ \frac{\sqrt{J_2}}{4} \frac{\partial}{\partial \tau} \left(-\sqrt{J_3 J_2} \frac{\partial u_\tau}{\partial \phi} + \sqrt{J_2} \frac{\partial u_\phi}{\partial \sigma} - \frac{J_{22}}{a J_{13}} u_\phi \right) \\ &+ \frac{J_{12}}{4a} \left(\sqrt{J_3 J_2} \frac{\partial u_\sigma}{\partial \phi} - \sqrt{J_2} \frac{\partial u_\phi}{\partial \sigma} + \frac{J_{12} u_\phi}{a} \right), \\ \chi_{\sigma\phi} = \chi_{\phi\sigma} &= \frac{\sqrt{J_2}}{4} \frac{\partial}{\partial \phi} \left(\sqrt{J_2} \left(\frac{\partial u_\tau}{\partial \sigma} - \frac{\partial u_\sigma}{\partial \tau} \right) + \frac{u_\sigma J_{13}}{a} - \frac{u_\tau J_{12}}{a} \right) \\ &+ \frac{\sqrt{J_3 J_2}}{4} \frac{\partial}{\partial \phi} \left(-\sqrt{J_3 J_2} \frac{\partial u_\tau}{\partial \phi} + \sqrt{J_2} \frac{\partial u_\phi}{\partial \tau} - \frac{J_{22}}{a J_{13}} u_\phi \right) \end{aligned}$$

$$\begin{aligned} &+ \frac{J_{12}}{4a} \left(\sqrt{J_2} \left(\frac{\partial u_\tau}{\partial \sigma} - \frac{\partial u_\sigma}{\partial \tau} \right) + \frac{u_\sigma J_{13}}{a} - \frac{u_\tau J_{12}}{a} \right), \\ \chi_{\tau\tau} &= \frac{\sqrt{J_2}}{2} \frac{\partial}{\partial \tau} \left(\sqrt{J_3 J_2} \frac{\partial u_\sigma}{\partial \phi} - \sqrt{J_2} \frac{\partial u_\phi}{\partial \sigma} + \frac{J_{12} u_\phi}{a} \right) \\ &- \frac{J_{12}}{2a} \left(-\sqrt{J_3 J_2} \frac{\partial u_\tau}{\partial \phi} + \sqrt{J_2} \frac{\partial u_\phi}{\partial \tau} - \frac{J_{22}}{a J_{13}} u_\phi \right), \\ \chi_{\tau\phi} = \chi_{\phi\tau} &= \frac{\sqrt{J_2}}{4} \frac{\partial}{\partial \tau} \left(\sqrt{J_2} \left(\frac{\partial u_\tau}{\partial \sigma} - \frac{\partial u_\sigma}{\partial \tau} \right) + \frac{J_{13} u_\sigma}{a} - \frac{J_{12} u_\tau}{a} \right) \\ &+ \frac{\sqrt{J_3 J_2}}{4} \frac{\partial}{\partial \phi} \left(\sqrt{J_3 J_2} \frac{\partial u_\sigma}{\partial \phi} - \sqrt{J_2} \frac{\partial u_\phi}{\partial \sigma} + \frac{J_{12} u_\phi}{a} \right) \\ &+ \frac{J_{14} J_{13}}{2a} \left(\sqrt{J_2} \left(\frac{\partial u_\tau}{\partial \sigma} - \frac{\partial u_\sigma}{\partial \tau} \right) + \frac{u_\sigma J_{13}}{a} - \frac{u_\tau J_{12}}{a} \right), \\ \chi_{\phi\phi} &= -\frac{J_{12}}{2a} \left(-\sqrt{J_3 J_2} \frac{\partial u_\tau}{\partial \phi} + \sqrt{J_2} \frac{\partial u_\phi}{\partial \tau} - \frac{J_{22}}{a J_{13}} u_\phi \right) \\ &- \frac{J_{14} J_{13}}{a} \left(\sqrt{J_3 J_2} \frac{\partial u_\sigma}{\partial \phi} - \sqrt{J_2} \frac{\partial u_\phi}{\partial \sigma} + \frac{J_{12} u_\phi}{a} \right) \\ &+ \frac{\sqrt{J_3 J_2}}{2} \frac{\partial}{\partial \phi} \left(\sqrt{J_2} \left(\frac{\partial u_\tau}{\partial \sigma} - \frac{\partial u_\sigma}{\partial \tau} \right) + u_\sigma \frac{J_{13}}{a} - u_\tau \frac{J_{12}}{a} \right) \end{aligned} \quad (20)$$

Consequently, the stress and the couple-stress tensor components are calculated employing the MCST stress-strain relation for isotropic bodies, i.e. $(t_{ij} = 2\mu(\epsilon_{ij} + l^2 \chi_{ij}) + \lambda \epsilon_{kk} \delta_{ij})$. It is worth mentioning that a vanishing length scale ($l = 0$) in the above governing reduces the non-classical couple stress theory to the conventional classical theory. To apply the boundary conditions, stress and strain tensors are required.

3.4. Boundary conditions

For a closed and hollow toroidal structure, the outer and interior surfaces should be traction-free. If the toroid is not closed, then the environmental stresses σ_ϕ should be zero in its open sections. In the following subsections, the boundary conditions for a fully closed, solid, and hollow toroidal shell are presented.

3.4.1. Boundary conditions for a closed and solid toroidal shell

The following boundary conditions are established for a fully closed and solid toroidal shell:

- (1) $\tau = \tau_0 : t_{\tau\tau} = 0$ or $2\mu(\epsilon_{\tau\tau} + l^2 \chi_{\tau\tau}) + \lambda I = 0$,
- (2) $\tau = \tau_0 : t_{\tau\sigma} = 0$ or $\epsilon_{\tau\sigma} + l^2 \chi_{\tau\sigma} = 0$,
- (3) $\tau = \tau_0 : t_{\tau\phi} = 0$ or $\epsilon_{\tau\phi} + l^2 \chi_{\tau\phi} = 0$

It is worth noting that the outer surface of a toroid is specified by $\tau = \tau_0$. In a 3D analysis for a toroidal shell with two ends clamped (CC), all the displacement components must be zero, i.e., $u_\sigma = u_\tau = u_\phi = 0$.

3.4.2. Boundary condition for a closed and hollow toroidal shell

For a fully closed and hollow toroidal shell, boundary conditions should be $t_{\tau\tau} = t_{\tau\sigma} = t_{\tau\phi} = 0$ at $\tau = \tau_i$, $\tau = \tau_o$ where τ_i shows the inner radius of the toroidal shell.

4. Helmholtz decomposition

In this section, Helmholtz decomposition is employed to generate the solution of elasticity problems in toroidal coordinates. Helmholtz decomposition, which includes the scalar and vector potentials, is one of the several different potential techniques that have been developed to solve the problems containing both displacement and stress variables [71]. This scheme provides a general solution for Navier's equations. Stress functions usually satisfy the equilibrium equations. When they are combined with the compatibility relations, a more tractable and straightforward system of equations is released. The Helmholtz theorem states that any sufficiently continuous differential vector field can be represented by the summation of a scalar potential gradient as an irrotational vector field (lamellar) and the curl of a

vector potential as a solenoidal vector field. Implementation of this representation for the displacement field leads to:

$$\mathbf{u} = \bar{\nabla}\Phi + \bar{\nabla} \times \Psi, \quad \bar{\nabla} \cdot \Psi = 0 \quad (22)$$

where Φ and Ψ are the Lamé potential functions. Four unknowns are required for the Helmholtz expression: one component for Φ and the other three components for Ψ . However, the vector \mathbf{u} only needs three components; hence, one condition is adjusted as $\bar{\nabla} \cdot \Psi = 0$. This condition states that there is no expansion wherever there is a rotation. Helmholtz decomposition is beneficial for the study of wave propagation problems. Since $\bar{\nabla} \cdot (\bar{\nabla} \times \Psi) = 0$, and \mathbf{u} is the vector field of small displacement, the vector potential Ψ does not appear in the volume change, i.e., $\bar{\nabla} \cdot \mathbf{u} = \bar{\nabla} \cdot \bar{\nabla}\Phi + \bar{\nabla} \cdot (\bar{\nabla} \times \Psi)$. Therefore, $I = \bar{\nabla} \cdot \mathbf{u} = \bar{\nabla}^2\Phi$ means that the dilatation is the Laplacian of the potential function Φ . If the rotation vector is shown with ω , then $\omega = \frac{1}{2}(\bar{\nabla} \times \mathbf{u})$. Since Φ is the non-rotational potential function, by applying the curl to Eq. (22), i.e. $\bar{\nabla} \times \mathbf{u} = \bar{\nabla} \times (\bar{\nabla}\Phi) + \bar{\nabla} \times (\bar{\nabla} \times \Psi)$, and knowing that $\bar{\nabla} \times (\bar{\nabla}\Phi)$ is zero, $\bar{\nabla} \times \mathbf{u} = \bar{\nabla} \times (\bar{\nabla} \times \Psi)$. On the other hand, $\bar{\nabla} \times (\bar{\nabla} \times \Psi) = \bar{\nabla}(\bar{\nabla} \cdot \Psi) - \bar{\nabla}^2\Psi$, hence, $\omega = -\frac{1}{2}\bar{\nabla}^2\Psi$. The substitution of Eq. (22) in the Navier's equation, i.e., Eq. (23) (see Ref. [4] for more details),

$$(\lambda + \mu)\bar{\nabla} \operatorname{div} \mathbf{u} + \mu\bar{\nabla}^2\mathbf{u} - \frac{1}{4}\mu l^2\bar{\nabla}^4\mathbf{u} = \rho\ddot{\mathbf{u}} \quad (23)$$

yields to $\bar{\nabla}(C_1^2\bar{\nabla}^2\Phi - \ddot{\Phi}) + \bar{\nabla} \times (C_2^2\left(1 - \left(\frac{l}{2}\right)^2\bar{\nabla}^2\right)\bar{\nabla}^2\Psi - \ddot{\Psi}) = 0$, where $\bar{\nabla}^4$ is the biharmonic operator $\bar{\nabla}^4 = \bar{\nabla}^2\bar{\nabla}^2$, v is the Poisson's coefficient, ρ is the material density, and \mathbf{u} is a 3D vector function representing the vibrational displacement field. A fully describing the governing equations of micro-torus structures in the toroidal coordinates with the material length scale is addressed in Ref. [4]. The Navier's equation can be written in the toroidal coordinates because Eq. (23) is independent of the coordinate system and can be used in the curvilinear coordinates. It can be proved that Navier's equation can be split into two equations:

$$C_1^2\bar{\nabla}^2\Phi = \ddot{\Phi}, \quad C_1^2 = (\lambda + 2\mu)/\rho, \quad (24)$$

$$C_2^2\left(1 - \left(\frac{l}{2}\right)^2\bar{\nabla}^2\right)\bar{\nabla}^2\Psi = \ddot{\Psi}, \quad C_2^2 = \mu/\rho \quad (25)$$

Waves with velocity C_1 are non-rotating waves, while waves propagated with the velocity C_2 are rotational (a wave in an elastic medium that causes an element of the medium to change its shape without a volume change). Eqs. (24) and (25) can be written in the toroidal coordinates using the obtained relationships.

4.1. Calculating displacement components using potential Φ and Ψ

By substituting Eqs. (6) and (12) into Eq. (22), the displacement components are calculated in terms of the two potential functions Φ and Ψ as follows:

$$\begin{aligned} \mathbf{u}_\sigma &= \frac{\cosh(\tau) - \cos(\sigma)}{a} \frac{\partial\Phi}{\partial\sigma} + \frac{(\cosh(\tau) - \cos(\sigma))}{a} \left(\frac{\partial\Psi_\phi}{\partial\tau} - \frac{1}{\sinh(\tau)} \frac{\partial\Psi_\tau}{\partial\phi} \right) \\ &\quad - \frac{\Psi_\phi(\cosh(\tau)\cos(\sigma) - 1)}{a\sinh(\tau)}, \\ \mathbf{u}_\tau &= \frac{\cosh(\tau) - \cos(\sigma)}{a} \frac{\partial\Phi}{\partial\tau} + \frac{\frac{\partial\Psi_\sigma}{\partial\phi}(\cosh(\tau) - \cos(\sigma))}{a\sinh(\tau)} \\ &\quad - \frac{(\cosh(\tau) - \cos(\sigma))\frac{\partial\Psi_\phi}{\partial\sigma} - \sin(\sigma)\Psi_\phi}{a}, \\ \mathbf{u}_\phi &= \frac{\cosh(\tau) - \cos(\sigma)}{a\sinh(\tau)} \frac{\partial\Phi}{\partial\phi} \\ &\quad + \frac{(\cosh(\tau) - \cos(\sigma))\left(\frac{\partial\Psi_\tau}{\partial\sigma} - \frac{\partial\Psi_\sigma}{\partial\tau}\right) + \Psi_\sigma \sinh(\tau) - \Psi_\tau \sin(\sigma)}{a} \end{aligned} \quad (26)$$

4.1.1. Separation of the expansion wave equation in the ϕ direction

Using Eqs. (24) and (8), the wave expansion equation is obtained as follows:

$$\begin{aligned} &\frac{\cos(\sigma) - \cosh(\tau)}{(a\sinh(\tau))^2} \left(-(\cosh(\tau) - \cos(\sigma)) \right. \\ &\times \left[\left(\frac{\partial^2\Phi}{\partial\sigma^2} + \frac{\partial^2\Phi}{\partial\tau^2} \right) (\sinh(\tau))^2 + \frac{\partial^2\Phi}{\partial\phi^2} \right] \\ &+ (\sinh(\tau))^2 \sin(\sigma) \frac{\partial\Phi}{\partial\sigma} + \sinh(\tau)(\cosh(\tau)\cos(\sigma) - 1) \frac{\partial\Phi}{\partial\tau} \Big) = \frac{1}{C_1^2} \frac{\partial^2\Phi}{\partial t^2} \end{aligned} \quad (27)$$

Here the decomposition of the variables is performed, but only the variable ϕ is decoupled. Hereof, the function Φ is considered as follows:

$$\Phi(\sigma, \tau, \phi, t) = H(\sigma, \tau)X(\phi)e^{i\omega t} \quad (28)$$

By substituting Eq. (28) into the equation of motion, i.e., Eq. (27), and some mathematical simplification, the governing equation for function $X(\phi)$ read:

$$\begin{aligned} \frac{1}{X(\phi)} \frac{d^2X(\phi)}{d\phi^2} &= -\kappa^2, \\ \kappa^2 &= \left(\frac{\omega a(\sinh(\tau))}{C_1(\cosh(\tau) - \cos(\sigma))} \right)^2 - \left(\frac{(\sinh(\tau))^2}{H(\sigma, \tau)(\cosh(\tau) - \cos(\sigma))} \right) \\ &\times \left(\sin(\sigma) \frac{\partial H(\sigma, \tau)}{\partial\sigma} - \frac{(1 - \cosh(\tau)\cos(\sigma))\partial H(\sigma, \tau)}{\sinh(\tau)\partial\tau} \right) \\ &+ \frac{(\sinh(\tau))^2}{H(\sigma, \tau)} \left(\frac{\partial^2 H(\sigma, \tau)}{\partial\sigma^2} + \frac{\partial^2 H(\sigma, \tau)}{\partial\tau^2} \right) \end{aligned} \quad (29)$$

Eq. (29) demonstrates that the function $X(\phi)$ is harmonic, and the solution is in terms of $\sin(\kappa\phi)$ and/or $\cos(\kappa\phi)$. On the other hand, the governing equation for the function $H(\sigma, \tau)$ is:

$$\begin{aligned} &\frac{\partial^2 H(\sigma, \tau)}{\partial\sigma^2} + \frac{\partial^2 H(\sigma, \tau)}{\partial\tau^2} - \frac{\sin(\sigma)}{(\cosh(\tau) - \cos(\sigma))} \frac{\partial H(\sigma, \tau)}{\partial\sigma} \\ &+ \frac{(1 - \cosh(\tau)\cos(\sigma))}{(\cosh(\tau) - \cos(\sigma))\sinh(\tau)} \frac{\partial H(\sigma, \tau)}{\partial\tau} \\ &+ \left(\left(\frac{\omega a}{C_1(\cosh(\tau) - \cos(\sigma))} \right)^2 - \frac{\kappa^2}{(\sinh(\tau))^2} \right) H(\sigma, \tau) = 0 \end{aligned} \quad (30)$$

The solution of Eq. (30) for $H(\sigma, \tau)$ and substituting the ensuing relation into Eq. (28) delivers the response of the non-rotational wave.

4.1.2. Separation of the rotational wave equation in ϕ direction

The rotational wave governing equation was presented by Eq. (25). Moreover, the Laplacian and biharmonic operators are expressed in the toroidal coordinates in Eqs. (14) and (A.1), respectively. Applying the condition $\bar{\nabla} \cdot \Psi = 0$ to Eq. (7) leads to:

$$\begin{aligned} \frac{\partial\Psi_\phi}{\partial\phi} &= \sinh(\tau) \left(-\frac{\partial\Psi_\sigma}{\partial\sigma} - \frac{\partial\Psi_\tau}{\partial\tau} \right) - \frac{2 - \cosh(\tau)(\cosh(\tau) + \cos(\sigma))}{\cosh(\tau) - \cos(\sigma)} \Psi_\tau \\ &\quad + \frac{2\sinh(\tau)\sin(\sigma)}{\cosh(\tau) - \cos(\sigma)} \Psi_\sigma \end{aligned} \quad (31)$$

According to the assumption of the separation of the variable ϕ , the following equations are obtained:

$$\begin{aligned} \Psi_\sigma(\sigma, \tau, \phi, t) &= H_1(\sigma, \tau)Y_1(\phi)e^{i\omega t}, \quad \Psi_\tau(\sigma, \tau, \phi, t) = H_2(\sigma, \tau)Y_2(\phi)e^{i\omega t} \quad \text{and} \\ \Psi_\phi(\sigma, \tau, \phi, t) &= H_3(\sigma, \tau)Y_3(\phi)e^{i\omega t} \end{aligned} \quad (32)$$

By substituting Eq. (32) into Eq. (31), we have:

$$\begin{aligned} H_3(\sigma, \tau) \frac{dY_3(\phi)}{d\phi} &= -J_{13}Y_1(\phi) \frac{\partial H_1(\sigma, \tau)}{\partial\sigma} - J_{13}Y_2(\phi) \frac{\partial H_2(\sigma, \tau)}{\partial\tau} \\ &\quad - E_1 H_2(\sigma, \tau)Y_2(\phi) \\ &\quad + E_2 H_1(\sigma, \tau)Y_1(\phi) \quad \text{and} \quad E_1 = \frac{2 - \cosh(\tau)(\cosh(\tau) + \cos(\sigma))}{\cosh(\tau) - \cos(\sigma)}, \\ E_2 &= \frac{2\sinh(\tau)\sin(\sigma)}{\cosh(\tau) - \cos(\sigma)} \end{aligned} \quad (33)$$

Employing Eq. (25) and the constraint equation, i.e., (33) and consideration of separation of the variables in Eq. (32), the equations of motion addressed in Supplementary Materials (B) in the σ, τ directions are obtained respectively from Ψ_σ and Ψ_τ . It is clear from Eqs. (B.1) and (B.2) that, if $Y_1(\phi) = \pm Y_2(\phi)$, the assumption of the separation of variables for the variable ϕ is acceptable and the function of $Y(\phi)$ is harmonically separable:

$$\frac{d^4 Y(\phi)}{d\phi^4} + \gamma^2 \frac{d^2 Y(\phi)}{d\phi^2} + \kappa^2 Y(\phi) = 0 \quad (34)$$

Eq. (33) demonstrates that $Y_3(\phi)$ should be chosen in such a way that the variable ϕ can be eliminated from both sides of this equation. In this case, the assumption of the separation of the variables would be acceptable. As described above, functions $Y(\phi)$ can be selected in each of the following forms:

$$\begin{aligned} (\text{I : }) \quad & Y_1(\phi) = Y_2(\phi) = \pm (\cosh(\wp_1\phi) - \sinh(\wp_1\phi)) \\ & \& Y_3(\phi) = \pm (\sinh(\wp_1\phi) - \cosh(\wp_1\phi)), \\ (\text{II : }) \quad & Y_1(\phi) = Y_2(\phi) = \pm (\cosh(\wp_1\phi) + \sinh(\wp_1\phi)) \\ & \& \& Y_3(\phi) = \pm (\sinh(\wp_1\phi) + \cosh(\wp_1\phi)), \\ (\text{III : }) \quad & Y_1(\phi) = Y_2(\phi) = \pm (\cosh(\wp_2\phi) - \sinh(\wp_2\phi)), \\ & \& \& Y_3(\phi) = \pm (\sinh(\wp_2\phi) - \cosh(\wp_2\phi)), \\ (\text{IV : }) \quad & Y_1(\phi) = Y_2(\phi) = \pm (\cosh(\wp_2\phi) + \sinh(\wp_2\phi)), \\ & \& \& Y_3(\phi) = \pm (\sinh(\wp_2\phi) + \cosh(\wp_2\phi)) \end{aligned} \quad (35)$$

where $\wp_1 = 1/2\sqrt{-2\gamma^2 - 2\sqrt{\gamma^4 - 4\kappa^2}}$, $\wp_2 = 1/2\sqrt{-2\gamma^2 + 2\sqrt{\gamma^4 - 4\kappa^2}}$. To avoid the complexity of the problem, the calculations would be continued assuming $X(\phi)$, and $Y_i(\phi)$, $i = 1, 2, 3$ as follows:

$$\begin{aligned} Y_1(\phi) &= Y_2(\phi) = \cosh(\wp_1\phi) - \sinh(\wp_1\phi), \\ Y_3(\phi) &= \sinh(\wp_1\phi) - \cosh(\wp_1\phi), X(\phi) = \cos(\kappa\phi) \end{aligned} \quad (36)$$

By applying Eqs. (32) and (36) to the displacement components, i.e., Eq. (26), the displacement components become:

$$\begin{aligned} u_\sigma &= \left(\sqrt{J_2} \frac{\partial H(\sigma, \tau)}{\partial \sigma} \cos(\kappa\phi) + \sqrt{J_2} \left(\frac{\partial H_3(\sigma, \tau)}{\partial \tau} (\sinh(\wp\phi) - \cosh(\wp\phi)) \right. \right. \\ &\quad \left. \left. - \frac{H_2(\sigma, \tau)}{J_{13}} \wp (\sinh(\wp\phi) - \cosh(\wp\phi)) \right) \right. \\ &\quad \left. - \frac{H_3(\sigma, \tau) (\sinh(\wp\phi) - \cosh(\wp\phi)) J_{22}}{a J_{13}} \right) e^{i\omega t}, \\ u_\tau &= \left(\sqrt{J_2} \frac{\partial H(\sigma, \tau)}{\partial \tau} \cos(\kappa\phi) + \sqrt{J_2 J_3} \wp (\sinh(\wp\phi) - \cosh(\wp\phi)) H_1(\sigma, \tau) \right. \\ &\quad \left. - \frac{(\sinh(\wp\phi) - \cosh(\wp\phi)) \left(S_2 \frac{\partial H_3(\sigma, \tau)}{\partial \sigma} - J_{12} H_3(\sigma, \tau) \right)}{a} \right) e^{i\omega t}, \\ u_\phi &= \left(-\kappa \sqrt{J_2 J_3} \sin(\kappa\phi) H(\sigma, \tau) + \frac{(\cosh(\wp\phi) - \sinh(\wp\phi))}{a} \right. \\ &\quad \left. \times \left(S_2 \left(\frac{\partial H_2(\sigma, \tau)}{\partial \sigma} - \frac{\partial H_1(\sigma, \tau)}{\partial \tau} \right) + H_1(\sigma, \tau) J_{13} - H_2(\sigma, \tau) J_{12} \right) \right) e^{i\omega t} \end{aligned} \quad (37)$$

After calculating the equations of motion and the displacement components, boundary conditions must be applied.

5. Solution method and results

Generally, practical engineering problems are complicated due to their geometry, material, and load discontinuities. A proper method is necessary to deal with them. In the following sections, different methods for investigation on different mechanical behaviors of toroidal structures are introduced.

5.1. Rayleigh-Ritz method to treat Navier's equations

It should be noted that an appropriate choice of a polynomial function in the Ritz method yields respectable convergence in responses of shell structures. Still, selecting these functions as a trial function creates a dynamic coupling, making the calculation more complicated. Choosing orthogonal polynomials is more effective than polynomial functions; because the selection of the orthogonal polynomials alongside their normalization transforms the mass matrix into a Unit Matrix, which consequently simplifies the problem. In the Ritz method, the energy equation, independent of its employed theory, is derived using the exact toroidal elasticity relations. Then admissible polynomials are implemented to treat the governing equations. More conveniently, Rayleigh's method can also be employed to determine the approximate fundamental natural frequency of a vibrating system without solving the governing differential equations of motion. Hence, if only the fundamental natural frequency of a system is needed, Rayleigh's technique should be employed. Otherwise, if several lowest natural frequencies of the system are required, the Rayleigh-Ritz method is preferred. The Rayleigh-Ritz method is an extension of Rayleigh's method. The Rayleigh-Ritz technique is based on the fact that Rayleigh's quotient gives an upper bound for the first eigenvalue, $\lambda_1 = \omega_1^2: R(X(x)) \geq \omega_1^2$, in which $X(x)$ is a trial function and the equality sign holds if and only if the trial function X coincides with the first eigenfunction of the system. In the Rayleigh-Ritz method, the normal linear mode of a system, i.e. $X(x)$, is approximated by a set of admissible functions that satisfy the geometric boundary conditions of a given problem $X(x) = \sum_{i=1}^n c_i \Xi_i(x)$ where c_i , $i = 1, 2, \dots, n$ are the Ritz coefficients, Moreover, $\Xi_i(x)$ are acceptable functions. The procedure is initiated by the determination of the strain and kinetic energies. The strain energy for an isotropic medium in volume \mathbb{V} is be calculated by [71,72]:

$$\begin{aligned} U &= \frac{1}{2} (\lambda + 2\mu) I^2 + 2\mu (\mathcal{E}_{\sigma\tau}^2 + \mathcal{E}_{\sigma\phi}^2 + \mathcal{E}_{\phi\tau}^2 - \mathcal{E}_{\sigma\sigma} \mathcal{E}_{\tau\tau} - \mathcal{E}_{\phi\phi} \mathcal{E}_{\sigma\sigma} - \mathcal{E}_{\phi\phi} \mathcal{E}_{\tau\tau}) \\ &\quad + \mu I^2 (\chi_{\sigma\sigma}^2 + \chi_{\tau\tau}^2 + \chi_{\phi\phi}^2 + 2\chi_{\sigma\tau}^2 + 2\chi_{\sigma\phi}^2 + 2\chi_{\phi\tau}^2) \end{aligned} \quad (38)$$

where I represents the dilatation or the expansion of the body, read [4]:

$$I = \sqrt{J_2} \left(\frac{\partial \mathbf{u}_\sigma}{\partial \sigma} + \frac{\partial \mathbf{u}_\tau}{\partial \tau} + \sqrt{J_3} \frac{\partial \mathbf{u}_\phi}{\partial \phi} \right) - \frac{2J_{12}}{a} \mathbf{u}_\sigma + \mathbf{u}_\tau q_{11} \quad (39)$$

in which coefficients J_i , q_i are defined in Supplementary Materials (A). The strain tensor, Eq. (19), and the curvature tensor, i.e., Eq. (20), are substituted into the strain energy to obtain displacement components. (As may be seen, strain energy consists of partial differential terms with non-linear coefficients, including trigonometric and hyperbolic functions that make the problem very complicated.) For undamped free vibration analysis, the displacement vector \mathbf{u}_i is harmonic in time. The Rayleigh-Ritz method employs the maximum strain energy U_{\max} , alongside the maximum kinetic energy T_{\max} , in a period of vibratory motion of a system. Strain energy would be maximized when the displacement of each point of a system reaches its maximum point during the motion, Hence, $\sin \omega t = 1$. The kinetic energy of a system is defined as follows:

$$T = \frac{1}{2} \rho \oint_{\mathbb{V}} (\dot{u}_\sigma^2 + \dot{u}_\tau^2 + \dot{u}_\phi^2) d\mathbb{V} \quad (40)$$

Assuming the time is harmonic, i.e. $\mathbf{u}_i(\sigma, \tau, \phi, t) \triangleq \bar{\mathbf{u}}_i(\sigma, \tau, \phi) \sin(\omega t)$, $i = \sigma, \tau, \phi$, the maximum kinetic energy is calculated as follows:

$$T_{\max} = \frac{1}{2} \rho \omega^2 \oint_{\mathbb{V}} (\bar{u}_\sigma^2 + \bar{u}_\tau^2 + \bar{u}_\phi^2) d\mathbb{V} \quad (41)$$

The trial functions are considered as follows:

$$\begin{aligned} \mathbf{u}_\sigma &= \sum_{i=0}^I \sum_{j=0}^J \sum_{k=0}^K A_{ijk} \mathfrak{A}_{ijk}(\sigma, \tau, \phi), \mathbf{u}_\tau = \sum_{m=0}^M \sum_{n=0}^N \sum_{p=0}^P B_{mnp} \mathfrak{B}_{mnp}(\sigma, \tau, \phi), \\ \mathbf{u}_\phi &= \sum_{q=0}^Q \sum_{r=0}^R \sum_{s=0}^S C_{qrs} \Gamma_{qrs}(\sigma, \tau, \phi) \end{aligned} \quad (42)$$

Furthermore, for generalization of the outcomes, some are introduced:

$$\begin{aligned} \aleph &= \frac{\tau}{\tau_R}, Y = \frac{\sigma}{\sigma_R}, \zeta = \frac{\phi}{\phi_R}, \quad d\tau = \tau_R d\aleph, \quad d\sigma = \sigma_R dY, \quad d\phi = \phi_R d\zeta \\ (43) \end{aligned}$$

wherein the reference values for a parameter or a variable are specified by the subscript R . Accordingly, the displacement components derivatives are calculated as follows:

$$\begin{aligned} \frac{\partial u_\tau}{\partial \tau} &= \frac{1}{\tau_R} \frac{\partial u_\tau}{\partial \aleph}, \quad \frac{\partial u_\tau}{\partial \sigma} = \frac{1}{\sigma_R} \frac{\partial u_\tau}{\partial Y}, \quad \frac{\partial u_\tau}{\partial \phi} = \frac{1}{\phi_R} \frac{\partial u_\tau}{\partial \zeta}, \\ \frac{\partial u_\sigma}{\partial \tau} &= \frac{1}{\tau_R} \frac{\partial u_\sigma}{\partial \aleph}, \quad \frac{\partial u_\sigma}{\partial \sigma} = \frac{1}{\sigma_R} \frac{\partial u_\sigma}{\partial Y}, \\ \frac{\partial u_\sigma}{\partial \phi} &= \frac{1}{\phi_R} \frac{\partial u_\sigma}{\partial \zeta}, \quad \frac{\partial u_\phi}{\partial \tau} = \frac{1}{\tau_R} \frac{\partial u_\phi}{\partial \aleph}, \quad \frac{\partial u_\phi}{\partial \sigma} = \frac{1}{\sigma_R} \frac{\partial u_\phi}{\partial Y}, \quad \frac{\partial u_\phi}{\partial \phi} = \frac{1}{\phi_R} \frac{\partial u_\phi}{\partial \zeta} \end{aligned} \quad (44)$$

The maximum kinetic energy in terms of the trial functions read:

$$\begin{aligned} T_{\max} &= \frac{\rho \omega^2}{2} \oint_V \left[\left(\sum_{i=0}^I \sum_{j=0}^J \sum_{k=0}^K A_{ijk} \mathfrak{A}_{ijk} (\aleph, Y, \zeta) \right)^2 \right. \\ &\quad + \left(\sum_{m=0}^M \sum_{n=0}^N \sum_{p=0}^P B_{mnp} \mathfrak{B}_{mnp} (\aleph, Y, \zeta) \right)^2 \\ &\quad \left. + \left(\sum_{q=0}^Q \sum_{r=0}^R \sum_{s=0}^S C_{qrs} \Gamma_{qrs} (\aleph, Y, \zeta) \right)^2 \right] dV, dV = h_\sigma \vec{e}_\sigma \cdot h_\tau \vec{e}_\tau \times h_\phi \vec{e}_\phi \end{aligned} \quad (45)$$

where ρ is density and ω shows natural frequency. In the toroidal coordinates, the parameter a is $a = d/2\coth(\tau)$, where $d = 2R$ is the diameter of the toroid, and R is the distance measured between the center of the torus and the center of the cross-section. The same procedure delivers the strain energy in terms of the trial functions, i.e., U_{\max} . The volume differential, i.e., $dV = \frac{d^3 \sinh^4(\tau) d\tau d\sigma d\phi}{8 \cosh^3(\tau) (\cosh(\tau) - \cos(\sigma))^3}$, in the orthogonal curvilinear coordinate system, can be computed employing Eq. (43)

$$dV = \left(\frac{d^3 \sinh^4(\tau_R \aleph)}{8 \cosh^3(\tau_R \aleph) (\cosh(\tau_R \aleph) - \cos(\sigma_R Y))^3} \right) \tau_R \sigma_R \phi_R d\aleph dY d\zeta \quad (46)$$

The maximum Lagrangian functional ($L_{\max} = U_{\max} - T_{\max}$) for the torus is obtained by setting $\sin^2(\omega t) = 1, \cos^2(\omega t) = 1$ in Eqs. (45) and (C.2). According to the Ritz technique process, minimizing the Lagrangian with respect to the arbitrary coefficients D_{ijk} , B_{mnp} , and C_{qrs} leads to:

$$\begin{aligned} \frac{\partial L}{\partial A_{ijk}} &= \sum_{i,j,k} D_{ijk} d_{1ijk} + \sum_{q,r,s} C_{qrs} c_{1qrs} \\ &+ \sum_{m,n,p} B_{mnp} b_{1mnp} - \Omega \sum_{i,j,k} A_{ijk} f_{1ijk} = 0, \\ \frac{\partial L}{\partial B_{mnp}} &= \sum_{i,j,k} D_{ijk} d_{2ijk} + \sum_{q,r,s} C_{qrs} c_{2qrs} + \sum_{m,n,p} B_{mnp} b_{2mnp} \\ &- \Omega \sum_{m,n,p} B_{mnp} f_{2mnp} = 0, \quad \Omega = \frac{\rho R^2 \omega^2}{(\lambda + 2\mu)} \\ \frac{\partial L}{\partial C_{qrs}} &= \sum_{i,j,k} D_{ijk} d_{3ijk} + \sum_{q,r,s} C_{qrs} c_{3qrs} + \sum_{m,n,p} B_{mnp} b_{3mnp} \\ &- \Omega \sum_{q,r,s} C_{qrs} f_{3qrs} = 0 \end{aligned} \quad (47)$$

Consequently, a set of $(i+1)(j+1)(k+1) + (m+1)(n+1)(p+1) + (q+1)(r+1)(s+1)$ linear, homogeneous, algebraic equations is obtained. The following relation should be presented in the matrix form:

$$\begin{aligned} \begin{bmatrix} [d_{1ijk}] & [b_{1mnp}] & [c_{1qrs}] \\ [d_{2ijk}] & [b_{2mnp}] & [c_{2qrs}] \\ [d_{3ijk}] & [b_{3mnp}] & [c_{3qrs}] \end{bmatrix} - \Omega \begin{bmatrix} [f_{1ijk}] & [0] & [0] \\ [0] & [f_{2mnp}] & [0] \\ [0] & [0] & [f_{3qrs}] \end{bmatrix} \begin{bmatrix} \{D_{ijk}\} \\ \{B_{mnp}\} \\ \{C_{qrs}\} \end{bmatrix} \\ = \begin{bmatrix} \{0\} \\ \{0\} \\ \{0\} \end{bmatrix} \end{aligned} \quad (48)$$

which can be considered as $([K] - \Omega [M])x = 0$, where K and M are the stiffness and mass matrices and $x = (D_{000}, D_{001}, \dots, D_{ijk}; B_{000}, B_{001}, \dots, B_{mnp}; C_{000}, C_{001}, \dots, C_{qrs})$. The polynomial and/or Fourier approximations can be selected for the trial functions. The Fourier approximation is a very useful tool for coordinates with periodic properties. Therefore, for the approximation of derivatives in the σ and ϕ directions, the Fourier approximation is implemented, while for the direction of τ , the polynomial approximation is employed. Combining these two approximations is an effective algorithm for the stress analysis in the toroidal coordinates system. For toroidal shells with a closed circular cross-section, there are two groups of circumferential vibration modes; one is symmetric. The other is asymmetric, and they can be analyzed independently because the symmetric and asymmetric vibrations are decoupled. The circumferential symmetric displacement field is approximated by the following Fourier series in both directions:

$$\sum_{i=0}^s \tau^i \sum_{m,n} (a_{uim} \sin(m\sigma) + b_{uimn} \cos(n\sigma)) \sum_{m,n} (c_{uipq} \sin(p\phi) + d_{uimn} \cos(q\phi)) \quad (49)$$

Considering Eq. (42) and using the assumptions $i = m = q, j = n = r, k = p = s$, the meridional, circumferential, and radial components of displacement can be approximated by the following Fourier series:

$$\begin{aligned} \mathfrak{R}_{mnp}(\sigma, \tau, \phi) &= \sum_{p=0}^P \sum_{n=0}^N \sum_{m=1}^M \underbrace{B_{Spmn}}_{\text{symmetric}} \cos(n\sigma) + \underbrace{B_{Apmn}}_{\text{anisymmetric}} \sin(n\sigma) \\ &\times Y'_m(\phi), \\ \mathfrak{S}_{mnp}(\sigma, \tau, \phi) &= \sum_{p=0}^P \sum_{n=0}^N \sum_{m=1}^M \underbrace{D_{Spmn}}_{\text{symmetric}} \sin(n\sigma) + \underbrace{D_{Apmn}}_{\text{anisymmetric}} \cos(n\sigma) \\ &\times Y_m(\phi), \\ \Gamma_{mnp}(\sigma, \tau, \phi) &= \sum_{p=0}^P \sum_{n=0}^N \sum_{m=1}^M \underbrace{C_{Spmn}}_{\text{symmetric}} \cos(n\sigma) + \underbrace{C_{Apmn}}_{\text{anisymmetric}} \sin(n\sigma) \\ &\times Y_m(\phi) \end{aligned} \quad (50)$$

where $Y_m(\phi)$ is the Euler–Bernoulli linear normal mode satisfies the boundary conditions, prime over a variable denotes the differential with respect to ϕ , and n is an integer number. D_{Spmn} and D_{Apmn} are the coefficient of the symmetric and asymmetric vibrations, respectively, which are orthogonal to each other. For the analysis of symmetric vibration, coefficients D_{Apmn} , B_{Apmn} and C_{Apmn} in the above equations are set to zero. However, for $n=0$, the displacement components reduce to $u_\tau = u_\phi = 0, u_\sigma = \sum_{p,n,m} \tau^p \underbrace{D_{Apmn}}_{\text{anisymmetric}} \cos(n\sigma) Y_m(\phi)$, which corresponds

to the torsional modes. A numerical example illustrates the effectiveness of the presented formulation and the solution. The model is an isotropic toroid with $E = 193$ GPa, $v = 0.291$, and $\rho = 7850$ kg/m³ [73]. The current first five natural frequencies versus the ABAQUS outcomes and the presented results from Ref. [73] are reported in Table 1. The results confirm the efficiency of the adopted approach in this paper. To consider the appearance of the modified couple stress theory in this research, the following results are provided in Table 1

As seen in Table 1, considering the length scale results in an increase in the natural frequencies for the toroidal shell

5.2. Solution of Laplace equation in Euclidean space in toroidal coordinates

In this section, we treat the Laplace equation stated on toroidal coordinates for the toroidal harmonics. The general solution of the Laplace equation $\bar{\nabla}^2 \psi$ in toroidal coordinates is known as a toroidal harmonic [74]. The toroidal harmonics is the name given to the solutions

Table 1First five natural frequencies of a thin CC toroid : Major radius = 0.1524 m, Minor radius = 0.056095 m, $h = 0.00211$ m.

Frequency [Hz]	Ritz method (Present work)	Wang et al. [73]	ABAQUS	Modified couple stress theory ($l/h = 0.01$)	Modified couple stress theory ($l/h = 0.02$)
A quarter torus					
f_1	3146.03	3147	3146.81	3150.13	3153.82
f_2	3410.22	3411	3408.80	3416.24	3418.05
f_3	3466.75	3468.04	3465.01	3469.11	3474.49
f_4	3596.81	3599	3595.21	3601.02	3604.91
f_5	3937.81	3943	3936.64	3942.85	3945.67
A half torus					
f_1	1278.27	1278	1278.61	1283.26	1286.1
f_2	2220.07	2216	2214.51	2224.98	2227.91
f_3	2384.83	2384	2384.64	2389.31	2392.73
f_4	2437.18	2429	2427.27	2442.16	2445.12
f_5	2450.37	2442	2440.31	2456.01	2458.36

of the Laplace equation in Euclidean space on toroidal coordinates. Although, initially, the equation seems to be not separable directly; however, an efficient trial solution is developed to treat it (The proposed solution is in terms of finite terms). The Laplacian in toroidal coordinates can be rewritten from Eq. (8) as follows:

$$\nabla^2 \Phi = \frac{(\cosh(\tau) - \cos(\sigma))^3}{a^2 \sinh(\tau)} \left[\sinh(\tau) \frac{\partial}{\partial \sigma} \left(\frac{1}{\cosh(\tau) - \cos(\sigma)} \frac{\partial \Phi}{\partial \sigma} \right) + \frac{\partial}{\partial \tau} \left(\frac{\sinh(\tau)}{\cosh(\tau) - \cos(\sigma)} \frac{\partial \Phi}{\partial \tau} \right) + \frac{1}{\sinh(\tau)(\cosh(\tau) - \cos(\sigma))} \frac{\partial^2 \Phi}{\partial \varphi^2} \right] \quad (51)$$

For the sake of brevity, the complete procedure is presented in Supplementary Materials (C). Accordingly, a general solution for the Laplace equation is:

$$\Phi = \sqrt{\cosh(\tau) - \cos(\sigma)} (c_1 e^{im\varphi} + c_2 e^{-im\varphi}) (c_3 e^{in\sigma} + c_4 e^{-in\sigma}) \\ \times (c_5 P_{n-1/2}^m(\cosh \tau) + c_6 Q_{n-1/2}^m(\cosh \tau)). \quad (52)$$

It is worth mentioning that the presented solution can be expressed in terms of toroidal harmonics, Legendre polynomials, or hypergeometric functions.

5.3. Electric potential due to a charged conducting torus

A study on the electric potential around the electrical tours is considered here; this problem needs solving the Laplace equation (Eq. (52)). The toroidal coordinates are related to the bipolar cylindrical coordinates by the transformation $(\rho, Z) = \left(\frac{a \sinh \tau}{\cosh \tau - \cos \sigma}, \frac{a \sin \sigma}{\cosh \tau - \cos \sigma} \right)$,

in which $a = 1$ is a geometric constant. The azimuthal angle ϕ is an identical variable in both coordinate systems. Let us assume $m = 0$, in Eq. (52) because the problem exhibits cylindrical symmetry; the solution leads to the relation for $T(\tau)$ (See Supplementary Materials (C) Eq. (C.15)). Consequently, the general symmetric harmonic solution in terms of the Eigen solutions, for cylindrical symmetry coordinates (bipolar coordinates), based on the real combinations of half-integer Legendre functions, as infinite series read:

$$\Phi = \sqrt{\cosh \tau - \cos \sigma} \times \sum_{n=0}^{\infty} [A_n P_{n-1/2}(\cosh \tau) + B_n Q_{n-1/2}(\cosh \tau)] \\ \times (a_n \cos n\sigma + b_n \sin n\sigma) \quad (53)$$

where, A_n and B_n are unknown coefficients, while P_n denotes Legendre polynomial of degree n [67]. It should be pointed out that the solution is for $\tau \geq 0$.

Some case studies are presented for more illustrations. We need a solution to be bounded in the domain $\tau_0 \leq \tau \leq \infty$; therefore, because

of the behavior of $P_{n-1/2}(\cosh \tau)$ and $Q_{n-1/2}(\cosh \tau)$ for large values of τ , we must specify A_n . On the other hand, for an exterior problem, which corresponds to the domain $0 \leq \tau < \tau_0$, we have to consider the behavior of $P_{n-1/2}(\cosh \tau)$ and $Q_{n-1/2}(\cosh \tau)$ when $\tau \rightarrow 0$. Moreover, we must pick B_n to have the solutions which remain bounded in the corresponding domain.

Case 1: Electric potential outside the torus

As shown in Fig. 1, the Z -axis is a special case when $\tau \rightarrow 0^+$. However, as the toroidal harmonics, i.e., $q_{mn}(\tau) \equiv Q_{n-1/2}^m(\cosh \tau)$ and $p_{mn}(\tau) \equiv P_{n-1/2}^m(\cosh \tau)$, are singular at points 1 and 0, respectively, as $\tau \rightarrow 0^+$, $Q_{n-1/2}(\cosh \tau)$ is too divergent at $\tau \rightarrow 0^+$. If the boundary condition $\Phi = \Phi_0$ (a constant) for $\tau = \tau_0$ (the toroidal surface) be an even function in σ , we must exclude terms including $(\sin \sigma)$; hence, the solution which satisfies the boundary condition of the outside of the torus read:

$$\Phi(\tau, \sigma) = \sqrt{\cosh \tau - \cos \sigma} \sum_{n=0}^{\infty} (A_n P_{n-1/2}(\cosh \tau)) \cos n\sigma \quad (54)$$

Moreover, the boundary condition $\Phi|_{\tau=\tau_0} = \Phi_0$ would be satisfied if we determine the coefficients A_n from the relation $\frac{\Phi_0}{\sqrt{\cosh \tau_0 - \cos \sigma}} = \sum_{n=0}^{\infty} A_n P_{n-1/2}(\cosh \tau_0) \cos n\sigma, -\pi \leq \sigma \leq \pi$. Imposing on Eq. (54), the boundary condition $\Phi = \Phi_0$ at $\tau = \tau_0$ and employing Eq. (55) yields to:

$$\pi = \sqrt{2(\cosh \tau_0 - \cos \sigma)} \sum_{n=0}^{\infty} (\lambda_n Q_{n-1/2}(\cosh \tau_0)) \cos n\sigma \quad (55)$$

where $\lambda_0 = 1$ and $\lambda_n = 2$ for $n > 0$. This relation is valid for any $\varphi \geq 1$, as well as any angle σ [75]. By considering $\varphi = \cosh(\tau_0)$, Eqs. (54) and (55) result in $A_n = \frac{\sqrt{2}\Phi_0}{\pi} \lambda_n \frac{Q_{n-1/2}(\cosh \tau_0)}{P_{n-1/2}(\cosh \tau_0)}$. Accordingly, the governing relation for Φ , outside the torus (along the circle $\tau = \tau_0$), at electric potential $\Phi = \Phi_0$ read:

$$\frac{\Phi(\tau, \sigma)}{\Phi_0} = \frac{\sqrt{2(\cosh \tau - \cos \sigma)}}{\pi} \sum_{n=0}^{\infty} \lambda_n \frac{Q_{n-1/2}(\cosh \tau_0)}{P_{n-1/2}(\cosh \tau_0)} \times (P_{n-1/2}(\cosh \tau)) \cos n\sigma \quad (56)$$

The convergence to the desired precision is acquired by increasing the magnitude of n . Once we have the solution for Φ , we can calculate $\bar{\nabla} \Phi$. Knowing that if the function Φ is differentiable, the gradient of the function Φ is either zero or perpendicular to the level set Φ at that point, we conclude that the level curves for Φ are orthogonal to $\bar{\nabla} \Phi$. As Φ is a function of σ and τ a transformation between bipolar cylindrical and Cartesian coordinates delivers $X =$

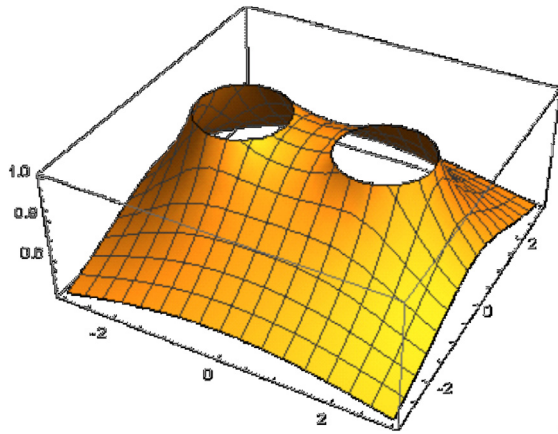


Fig. 2. Electric potential outside the torus on its reference circle $\tau_0 = 1$ (Case 1).

$\frac{\sinh \tau}{\cosh \tau - \cos \sigma}$, and $Y = \frac{\sin \sigma}{\cosh \tau - \cos \sigma}$. The corresponding inverse transformation denoted by $\sigma = \tan^{-1} \frac{2Y}{X^2 + Y^2 - 1}$, and $\tau = \tanh^{-1} \frac{2X}{X^2 + Y^2 + 1}$.

The scale factors for bipolar and Cartesian coordinates are identically defined by $h_\sigma = h_\tau = h = \frac{1}{\cosh \tau - \cos \sigma}$. The local orthonormal basis

vectors are related to the standard Cartesian basis vectors, according to $\mathbf{a}_\sigma = h(-(\sin \sigma \sinh \tau) \mathbf{a}_X + (\cos \sigma \cosh \tau - 1) \mathbf{a}_Y)$, and $\mathbf{a}_\tau = h(-(\cos \sigma \cosh \tau - 1) \mathbf{a}_X - (\sin \sigma \sinh \tau) \mathbf{a}_Y)$. A convergence study is performed to find out how many terms deliver our desired precision. The outcomes demonstrate that five terms are enough for our study. Fig. 2 illustrates the function Φ/Φ_0 for $\tau_0 = 1$, showing how the potential drops a bit in the center of the torus. The boundary condition which gives rise to the Fourier series is $\Phi/\Phi_0 = 1$ along the circle $\tau = \tau_0$.

Because the scale factors for both coordinates are similar, the gradient of the potential function is $\bar{\nabla}\Phi = \frac{1}{h} \left(\frac{\partial \Phi}{\partial \sigma} \mathbf{a}_\sigma + \frac{\partial \Phi}{\partial \tau} \mathbf{a}_\tau \right)$. Fig. 3

demonstrates various lines related to the electric potential on a torus based on the function $\bar{\nabla}\Phi$. This Figure shows field lines (solid blue lines). It can be seen that $\bar{\nabla}\Phi$ is perpendicular to the torus (Look at the field lines; everywhere, they are perpendicular to the contour lines of the electric potential). As we assumed that $\Phi = \Phi_0 = \text{const}$, it is interesting that regions where $|\bar{\nabla}\Phi| = 0$ be on the surface of the torus (exactly vanishing field lines on the total surface of the torus). When $\tau \rightarrow 0$ geometrically speaking, the system treats like a cylinder, just curled into a torus. In this case, the singularity of the electrical field is in its strongest situation, occurred at the center point (0,0,0). As shown in Fig. 2, the field looks like two parallel infinitely long cylinders in a perpendicular field that do not feel each other in the XZ plane. The electric potential between two tori (with the same reference circle $r = a$, $Z = 0$) held at different electric potential levels can be expressed as:

$$\frac{\Phi(\tau, \sigma)}{\sqrt{\cosh \tau - \cos \sigma}} = \sum_{n=0}^{\infty} (a_n P_{n-1/2}(\cosh \tau) + b_n Q_{n-1/2}(\cosh \tau)) \cos n\sigma \quad (57)$$

where the coefficients a_n and b_n can be determined via the use of Eq. (55), and solving two linear equations, arising from $\Phi = \Phi_0$ at $\tau = \tau_0$ and $\Phi = \Phi_1$ at $\tau = \tau_1$, which lead to Eqs. (58) and (59).

$$\begin{aligned} \frac{\Phi_0(\tau_0, \sigma)}{\sqrt{\cosh \tau_0 - \cos \sigma}} &= \sum_{n=0}^{\infty} (a_n P_{n-1/2}(\cosh \tau_0) + b_n Q_{n-1/2}(\cosh \tau_0)) \cos n\sigma \\ &= \sum_{n=0}^{\infty} c_n \cos n\sigma \end{aligned} \quad (58)$$

$$\begin{aligned} \frac{\Phi_1(\tau_1, \sigma)}{\sqrt{\cosh \tau_1 - \cos \sigma}} &= \sum_{n=0}^{\infty} (a_n P_{n-1/2}(\cosh \tau_1) + b_n Q_{n-1/2}(\cosh \tau_1)) \cos n\sigma \\ &= \sum_{n=0}^{\infty} d_n \cos n\sigma \end{aligned} \quad (59)$$

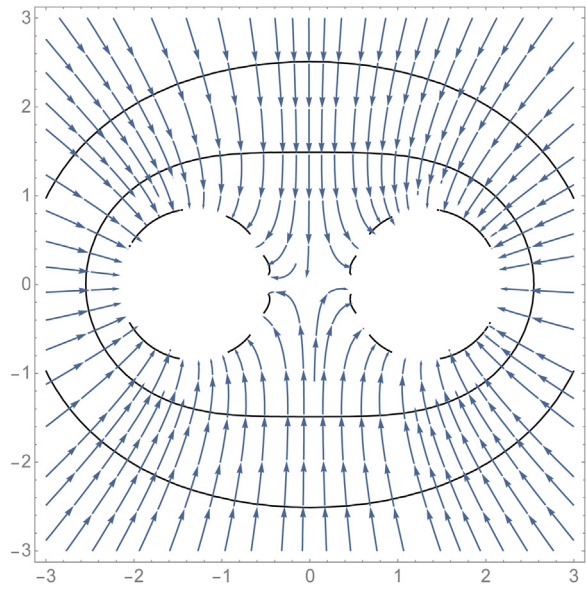


Fig. 3. Schematic representation of $\bar{\nabla}\Phi$ and $\tau_0 = 1$ (Case1) . (For interpretation of the references to color in this figure legend, the reader is referred to the web version of this article.)

Comparing Eq. (55) with (58) considering the fact of the uniqueness of the Fourier coefficients, deliver to us:

$$c_n = \frac{\Phi_0 \sqrt{2}}{\pi} \hat{\lambda}_n Q_{n-1/2}(\cosh \tau_0) \quad (60)$$

Similarly, $d_n = \frac{\Phi_1 \sqrt{2}}{\pi} \hat{\lambda}_n Q_{n-1/2}(\cosh \tau_1)$. Moreover, because of Eqs. (58) and (59) are applicable independent of n , we have:

$$\begin{bmatrix} P_{n-1/2}(\cosh \tau_0) & Q_{n-1/2}(\cosh \tau_0) \\ P_{n-1/2}(\cosh \tau_1) & Q_{n-1/2}(\cosh \tau_1) \end{bmatrix} \begin{bmatrix} A_n \\ B_n \end{bmatrix} = \begin{bmatrix} \Phi_0 Q_{n-1/2}(\cosh \tau_0) \\ \Phi_1 Q_{n-1/2}(\cosh \tau_1) \end{bmatrix} \quad (61)$$

where $a_n = \frac{\sqrt{2} \hat{\lambda}_n}{\pi} A_n$ and $b_n = \frac{\sqrt{2} \hat{\lambda}_n}{\pi} B_n$. Furthermore, a_n and b_n are determined by the implementation of Eq. (61); $a_n = \frac{\sqrt{2} \hat{\lambda}_n}{\pi} \frac{A_A}{\Delta}$, $b_n = \frac{\sqrt{2} \hat{\lambda}_n}{\pi} \frac{A_B}{\Delta}$, where

$$\begin{aligned} \Delta &= \begin{vmatrix} p_{n-1/2}(\cosh \tau_0) & Q_{n-1/2}(\cosh \tau_0) \\ p_{n-1/2}(\cosh \tau_1) & Q_{n-1/2}(\cosh \tau_1) \end{vmatrix}, \\ A_A &= \begin{vmatrix} \Phi_0 Q_{n-1/2}(\cosh \tau_0) & Q_{n-1/2}(\cosh \tau_0) \\ \Phi_1 Q_{n-1/2}(\cosh \tau_1) & Q_{n-1/2}(\cosh \tau_1) \end{vmatrix}, \\ A_B &= \begin{vmatrix} p_{n-1/2}(\cosh \tau_0) & \Phi_0 Q_{n-1/2}(\cosh \tau_0) \\ p_{n-1/2}(\cosh \tau_1) & \Phi_1 Q_{n-1/2}(\cosh \tau_1) \end{vmatrix} \end{aligned} \quad (62)$$

Fig. 4 illustrates the schematic representation of the function Φ for two different tori. Comparing Fig. 4a and b, it can be conducted that for a thinner torus (larger τ_0), the potential drops more in the toroid center.

Case 2 : Potential charge on the reference circle inside a torus

We start from Eq. (63) to deal with a potential charge on the reference circle inside a torus (toroidal coordinates with the ring as its reference circle) with constant τ , say $\tau = \tau_0$. For a uniform distribution of potential charge on the reference circle, the potential charge at ($Z = 0, r = a$) is

$$\Phi(\tau, \sigma) = \sqrt{\cosh \tau - \cos \sigma} \left(P_{-1/2}(\cosh \tau) - \frac{Q_{-1/2}(\cosh \tau) P_{-1/2}(\cosh \tau_0)}{Q_{-1/2}(\cosh \tau_0)} \right) \quad (63)$$

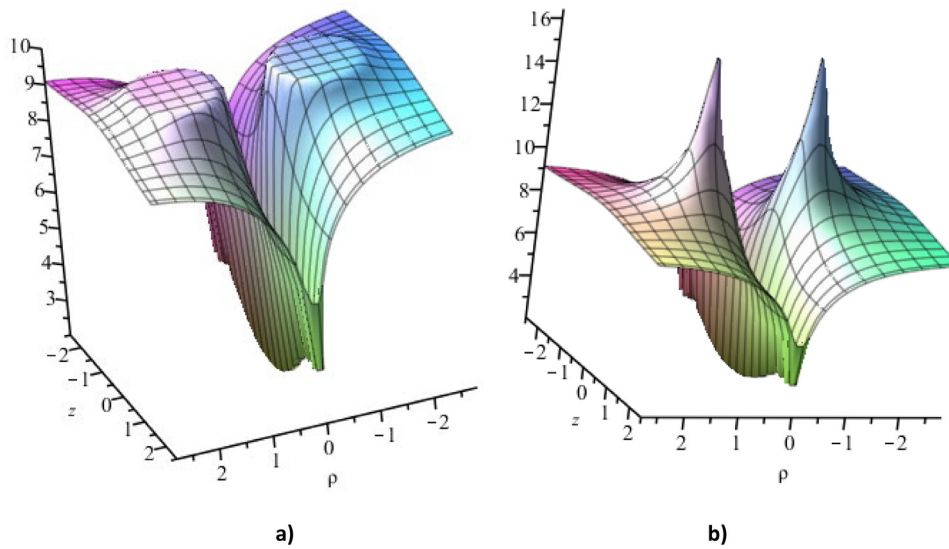


Fig. 4. Schematic representation of Φ for $N = 100$ (Case1) (a) $\tau_0 = 1, \tau_1 = 5, \Phi_0 = 10$, and $\Phi_1 = 20$ (b) $\tau_0 = 5, \tau_1 = 1, \Phi_0 = 20$, and $\Phi_1 = 10$.

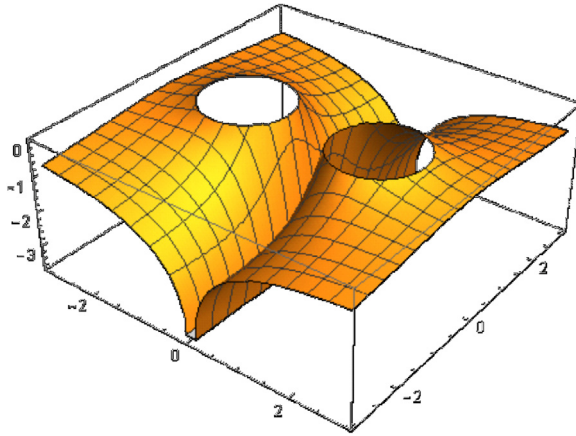


Fig. 5. Potential charge on the reference circle inside a torus ($\tau_0 = 1$ (Case2)).

The line-charge potential density can be deduced from the logarithmic singularity in $P_{1/2}(\cosh \tau)$ at the ring. It should be noted that continuity of the potential at $\phi = 2\pi$ requires that m be an integer number. The simplest case is when $m = 0$. In this case, the potential charge has no dependency on the azimuthal angle ϕ . The boundary conditions do not depend on σ , and ϕ . Moreover, the Laplace equation vanishes at $\tau = \tau_0$ while it possesses the same logarithmic singularity on the reference circle. Figs. 5 and 6 illustrate the schematic representation of the functions Φ and $\bar{\nabla}\Phi$, respectively.

Case 3: Potential of the reference circle inside a torus (a uniform line dipole potential)

Similarly, for a uniform line dipole charge density around the reference circle inside the torus, the potential charge read:

$$\Phi(\tau, \sigma) = \sqrt{\cosh \tau - \cos \sigma} \left(P_{1/2}(\cosh \tau) - \frac{Q_{1/2}(\cosh \tau)P_{1/2}(\cosh \tau_0)}{Q_{1/2}(\cosh \tau_0)} \right) \times \cos(\sigma - \sigma_0) \quad (64)$$

where arbitrary σ_0 corresponds to the orientation of the dipole variations. Figs. 7 and 8 demonstrate the schematic representation of the function Φ and $\bar{\nabla}\Phi$, respectively.

Case 4: Equipotentials in the axial plane for axial electrical excitation

In this case, the Laplace equation is treated with the consideration of the following boundary conditions:

$$\Phi(X, Y, Z) \rightarrow Z, \quad X, Y, Z \gg R, \quad \vec{n} \cdot \bar{\nabla}\Phi(X, Y, Z)|_{\text{torus}} = 0 \quad (65)$$

Eq. (65) shows that the assumed boundary condition on the torus is regarded to be free; in other words, the vector normal to the mesh boundary at each point would be equal to zero. Hence, we seek the solution for some kind of potential charge Φ which far from the torus it approaches to the linearly increasing function $\Phi = Z$. Accordingly, $\bar{\nabla}\Phi$ is parallel to the surface of the torus. So, $\bar{\nabla}\Phi$ gives a vector field that simulates potential inviscid (irrotational) around the torus. Alternatively, if the torus is perfectly diamagnetic, then the magnetic field outside the torus is given by $\bar{\nabla}\Phi$. The total potential charge must vanish on the conducting boundaries, i.e. $\tau = \tau_0$. The obvious odd symmetry in the Z direction is transformed into odd symmetry in the σ direction. An appropriate expansion for the scattered potential charge in the outer region $0 \leq \tau \leq \tau_0, -\pi \leq \sigma \leq \pi$ is [76]:

$$\Phi(\tau, \sigma) = \Phi_0 \sqrt{2a} \sqrt{\cosh \tau - \cos \sigma} \sum_{n=1}^{\infty} a_n \frac{P_{n-1/2}(\cosh \tau)}{P_{n-1/2}(\cosh \tau_0)} \sin n\sigma \quad (66)$$

Furthermore, the Dirichlet boundary condition is;

$$\Phi(\tau_0, \sigma) = \Phi_0 Z = \Phi_0 a \frac{\sin \sigma}{\cosh \tau_0 - \cos \sigma} \quad (67)$$

Therefore, a Fourier sine series in the following form is required

$$\frac{\sin \sigma}{(2 \cosh \tau_0 - 2 \cos \sigma)^{3/2}} = \sum_{n=1}^{\infty} b_n \sin n\sigma \quad (68)$$

The Fourier coefficients b_n are defined by an integral representation as follows:

$$\begin{aligned} Q_{n-1/2}(\cosh \tau) &= \int_0^\pi \frac{\cos n\zeta}{[2 \cosh \tau - 2 \cos \zeta]^{1/2}} d\zeta \\ &= \frac{1}{n} \int_0^\pi \frac{\sin n\zeta \sin \zeta}{[2 \cosh \tau - 2 \cos \zeta]^{3/2}} d\zeta \end{aligned} \quad (69)$$

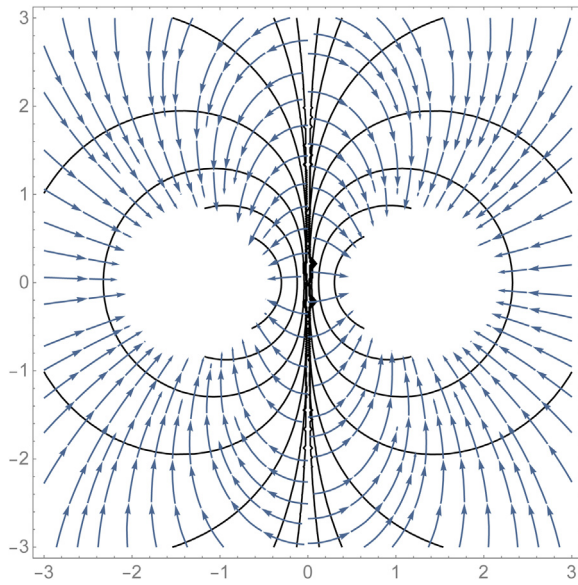


Fig. 6. Schematic representation obtained for $\bar{\nabla}\Phi$ and $\tau_0 = 1$ (Case 2).

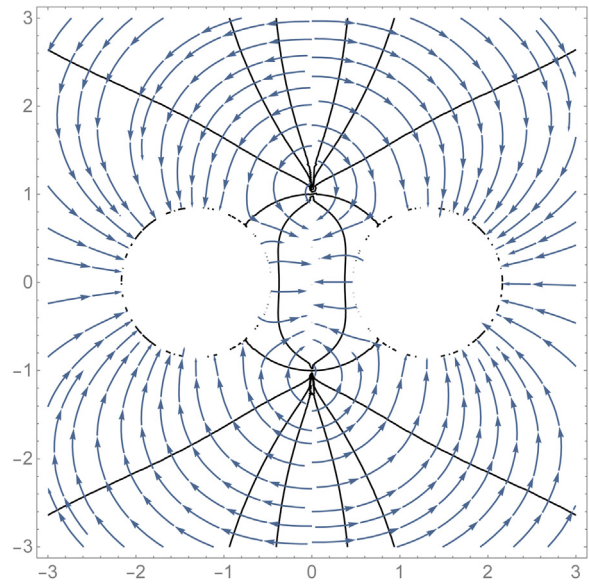


Fig. 8. Schematic representation of $\bar{\nabla}\Phi$ obtained for $\tau_0 = 1$ and $\sigma_0 = 0$ (Case 3).

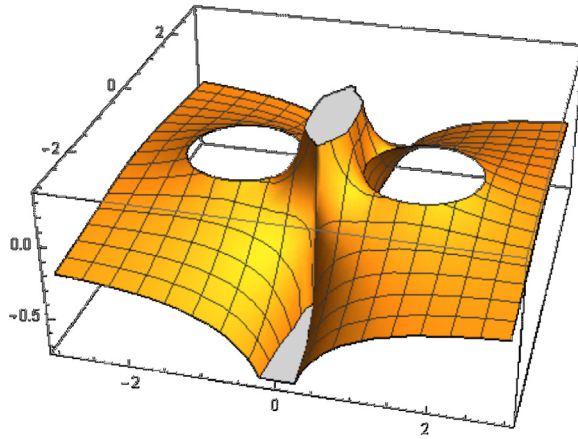


Fig. 7. Potential charge of the reference circle inside a torus (a uniform line dipole potential) $\tau_0 = 1$ and $\sigma_0 = 0$ (Case 3).

In this case, the total potential can be written as:

$$\frac{\Phi(\tau, \sigma)}{\Phi_0} = \frac{4a\sqrt{2}}{\pi} \sqrt{\cosh \tau - \cos \sigma} \times \sum_{n=1}^{\infty} \frac{Q_{n-1/2}(\cosh \tau) P_{n-1/2}(\cosh \tau) - Q_{n-1/2}(\cosh \tau) P_{n-1/2}(\cosh \tau)}{P_{n-1/2}(\cosh \tau)} \times \sin n\sigma \quad (70)$$

By implementing Eq. (70), the equipotential contours are depicted in Fig. 9 for a reasonably fat ($\frac{R}{\rho_c} = 0.8$) toroid (R is the tube radius).

The toroidal surface of Fig. 9 is the surface of constant $\tau = \tau_0$, and $-\pi \leq (\sigma, \phi) \leq \pi$ with the original dimensions of the toroid as $\rho_c = a \coth \tau_0$, $R = a \operatorname{csch} \tau_0$, $\tau_0 = \cosh^{-1} \left(\frac{\rho_c}{R} \right)$, and $a = \sqrt{\rho_c^2 - R^2}$ where the tube center is located in the distance ρ_c from the Z-axis, $\tau = \arctan h \left(2\rho_c \frac{|\rho|}{\rho^2 + Z^2 + \rho_c^2}, 2Z\rho_c \right)$ where $\rho = \sqrt{X^2 + Y^2}$ and $\sigma = \arctan 2\pi$ $(\rho^2 + Z^2 - \rho_c^2, 2Z\rho_c)$. The series that appeared in Eq. (70) has reasonably rapid convergence because of the nature of these potential solutions. Here 200 terms are sufficient to reach the numerical convergency.

Case 5: Torus surface charge density

In this case, a discussion is presented on the torus surface charge density. The torus surface charge density may be obtained from the potential charge:

$$\Pi = \frac{1}{4\pi} \left(1/h_{\tau_0} \right) \left[\frac{\partial \Phi(\tau, \sigma)}{\partial \tau} \right] \Big|_{\tau=\tau_0}, \quad 1/h_{\tau_0} = (\cosh \tau_0 - \cos \sigma) / a \quad (71)$$

By the implementation of Eq. (56), Eq. (71) converts to:

$$\begin{aligned} \Pi = & \frac{\Phi_0 \sqrt{2}}{4\pi^2} \sum_{n=0}^{\infty} \frac{\epsilon_n Q_{n-1/2}(\cosh \tau_0) \cos(n\sigma)}{h_{\tau_0} P_{n-1/2}(\cosh \tau_0)} \\ & \times \partial_\tau \left[\sqrt{\cosh \tau - \cos \sigma} P_{n-1/2}(\cosh \tau) \right] \Big|_{\tau=\tau_0} \end{aligned} \quad (72)$$

$$\begin{aligned} \text{We need then to compute, } & \frac{1}{h_{\tau_0}} \partial_\tau \left[\sqrt{\cosh \tau - \cos \sigma} P_{n-1/2}(\cosh \tau) \right] \Big|_{\tau=\tau_0} \text{ as:} \\ & \frac{1}{h_{\tau_0}} \partial_\tau \left[\sqrt{\cosh \tau - \cos \sigma} P_{n-1/2}(\cosh \tau) \right] \Big|_{\tau=\tau_0} = \frac{\sinh \tau_0}{a} \\ & \left[(\cosh \tau_0 - \cos \sigma)^{\frac{3}{2}} P'_{n-1/2}(\cosh \tau_0) + (1/2) \left(\sqrt{\cosh \tau_0 - \cos \sigma} \right) \right. \\ & \left. \times P_{n-1/2}(\cosh \tau_0) \right] \end{aligned} \quad (73)$$

Inserting the equation mentioned above into Eq. (72) and employing $\frac{\sinh \tau_0}{a} = \frac{1}{R}$ leads to:

$$\begin{aligned} \Pi = & \frac{\sqrt{2}}{4\pi^2 R} \Phi_0 \sum_{n=0}^{\infty} \epsilon_n \frac{Q_{n-1/2}(\cosh \tau_0)}{P_{n-1/2}(\cosh \tau_0)} \cos(n\sigma) \times \\ & \left[(\cosh \tau_0 - \cos \sigma)^{3/2} P'_{n-1/2}(\cosh \tau_0) + (1/2) \sqrt{\cosh \tau_0 - \cos \sigma} \right. \\ & \left. \times P_{n-1/2}(\cosh \tau_0) \right] \end{aligned} \quad (74)$$

The simplification results in:

$$\begin{aligned} \Pi(\sigma; \tau_0) = & \frac{\Phi_0}{4\pi R} \left(\frac{1}{2} + \frac{\sqrt{2}}{\pi} (\cosh \tau_0 - \cos \sigma)^{3/2} \sum_{n=0}^{\infty} \epsilon_n P'_{n-1/2} \right. \\ & \left. \times (\cosh \tau_0) \frac{Q_{n-1/2}(\cosh \tau_0)}{P_{n-1/2}(\cosh \tau_0)} \cos(n\sigma) \right) \end{aligned} \quad (75)$$

Eq. (75) defines the torus surface charge density with tube radius R and τ_0 at the potential Φ_0 . Figs. 10 and 11 represent the schematic of the functions Π and $\bar{\nabla}\Pi$, respectively. The surface charge against the

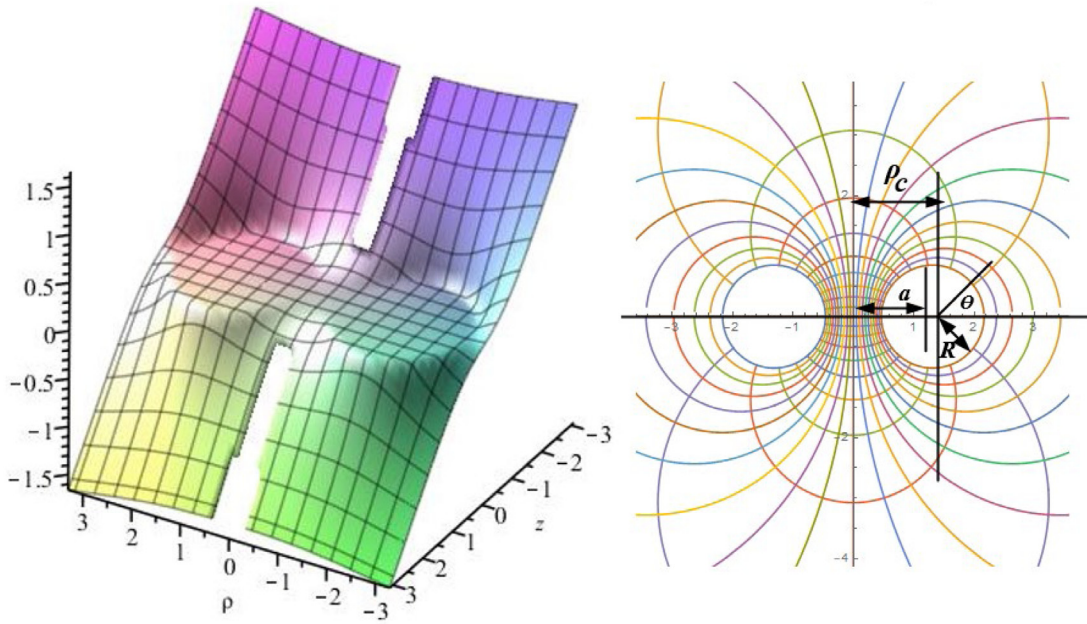


Fig. 9. Equipotentials in the axial plane for axial electrical excitation Z: $\rho_c = 1$ and $R = 0.8$ (Case 4).

circle angle θ for a torus cross-section is depicted in see Fig. 9. In this respect, an expression defining the total charge dQ in a patch of area dA on the torus has been considered:

$$dQ = \Pi dA = \Pi (h_\sigma d\sigma) (h_\phi d\phi) = \Pi h_\sigma h_\phi \frac{d\sigma}{d\theta} d\theta d\phi \quad (76)$$

$h_\sigma h_\phi$ can be obtained by using $(\rho - \rho_c)^2 + Z^2 = R^2$, and $h = \frac{a}{\cosh \tau - \cos \sigma} = a \frac{\cosh \tau + \cos \theta}{\sinh^2 \tau}$ as $h_\sigma h_\phi = \frac{a^2 (\cosh \tau + \cos \theta)^2}{\sinh^3 \tau}$. Employing $\frac{d\sigma}{d\theta} = \frac{\sinh \tau}{\cosh \tau + \cos \theta}$ along side with Eq. (76), we have, now setting $\tau = \tau_0$ (torus label):

$$\frac{dQ_\theta}{d\theta d\phi} = \Pi R^2 (\cosh \xi_0 + \cos \theta) \quad (77)$$

Letting N being the number of terms included in the summation process, from Eq. (75), the charge density Π read:

$$\begin{aligned} \Pi(N) &= \frac{\Phi_0}{4\pi R} \left(\frac{1}{2} + \frac{\sqrt{2}}{\pi} (\cosh \tau_0 - \cos \sigma)^{3/2} \sum_{n=0}^N \epsilon_n P'_{n-1/2} \right. \\ &\quad \times \left. (\cosh \tau_0) \frac{Q_{n-1/2} (\cosh \tau_0)}{P_{n-1/2} (\cosh \tau_0)} \cos(n\sigma) \right) \end{aligned} \quad (78)$$

It is easy to replace the $(\cosh \tau_0 - \cos \sigma)^{3/2}$ factor in Eq. (78) in terms of σ and θ using $\cosh \tau - \cos \sigma = \frac{\sinh^2 \tau}{\cosh \tau + \cos \theta}$. The trend dQ_θ in terms of θ for various τ_0 is depicted in Fig. 12. These plots are normalized to have $dQ_\theta(0) = 1$ on the outer equator of the torus. Since $\cos(n\sigma) \sim 1$, the main idea in the $dQ(\theta)$ summation process is that near $[\theta = 0$ i.e., outer equator ($\sigma = 0$)] the terms are additive. Nonetheless, in the “backward direction”, especially near $[\theta = \pi$ i.e., inner equator ($\sigma = \pi$)], there is a term interference from $\cos(n\sigma) \sim (-1)^n$ which causes the charge to be concentrated on the outer toroidal surface, just as one would expect. This situation is akin to the forward peak in a scattering amplitude in partial wave analysis. For $\tau_0 = 5$ the torus is close to the thin-wire limit, so dQ is practically uniform in θ as indicated by the top curve ($\tau_0 = 5$) in Fig. 12. Once again, the thin wire is an isolated infinite straight wire that naturally has a uniform θ . As the tori get fatter, the dQ distribution becomes more peaked at $\theta = 0$. In all cases, the peak value for dQ occurs on the outside equator $\theta = 0$. Hence, one can regard the bottom curve ($\tau_0 = 0.15$) in Fig. 12 as the “fat toroid limit” and the top curve ($\tau_0 = 5$) as the “thin toroid limit”. The torus charge density is finite and smooth everywhere because a torus has no sharp edges.

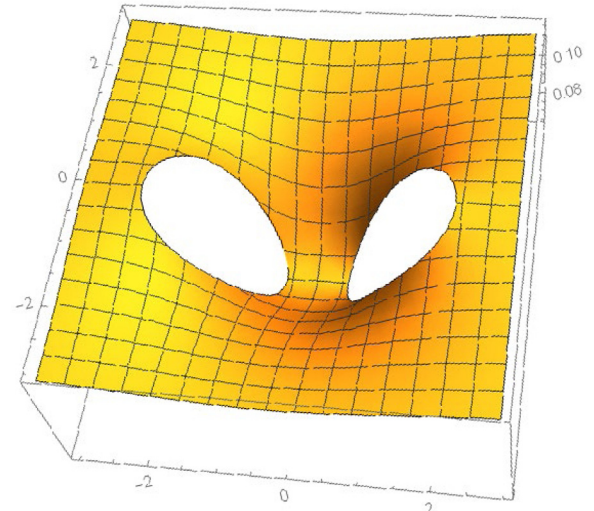


Fig. 10. Surface charge density on a torus with $\Phi_0 = R = 1$ and $N = 20$ (Case5).

In general, the torus σ drops monotonically from its maximum value on the outer equator to some finite values on the inner equator. The charge density on the inside surface of the toroid is zero.

5.4. Wave equation in a micro torus

If the toroidal surface has covered through a thin layer of some fluid, to describe the motion of the surface of the fluid along $\Omega \in \mathbb{R}^n$, treating the wave equation $\nabla^2 \Phi = \zeta \frac{\partial^2 \Phi}{\partial t^2}$, $\zeta = \frac{\rho}{(A+2\mu)}$ is necessary. In this relation Φ represents the height of the wave above the point (τ, σ, ϕ) at time t . Furthermore, the domain Ω is the torus membrane, where its boundary $\partial\Omega$ has been attached to the rim of the torus. For studying the vibration of torus structures, we should be certain about taking into account that the border of the membrane is fixed. Moreover, the solutions should have the capability to satisfy $\Phi(\tau, \sigma, \phi, t) = 0$ for all points on the boundary $\partial\Omega(\tau, \sigma, \phi, t) = 0$. Given an arbitrary manifold domain Ω with boundary $\partial\Omega$, one may impose two essential boundary

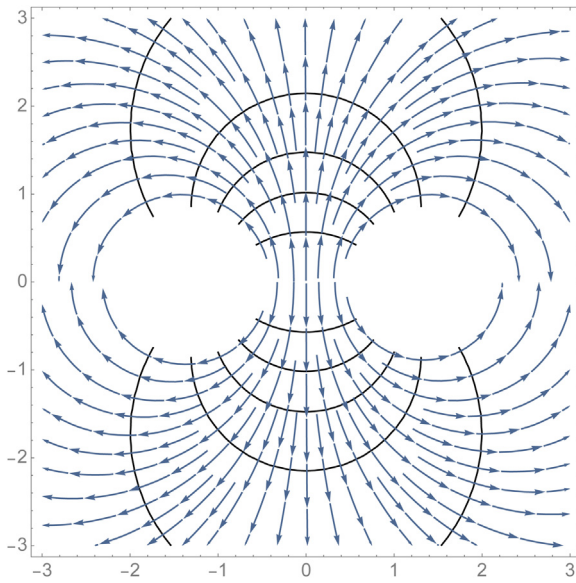


Fig. 11. Schematic representation obtained for $\bar{\nabla}H(\Phi_0 = R = 1, \text{and } N = 20 \text{ (Case5)})$.

conditions on the solutions of the eigenvalue problem $\Delta\Phi = \lambda\Phi$. The first one is the Dirichlet boundary condition type, which is used, for instance, when the domain $\Omega \in \mathbb{R}^n$ is a membrane, and its boundary is fixed. Since there are no vibrations on the rim of a torus, $\Phi|_{\partial\Omega} = 0$ must be applied to the solution. The second case is the Neumann boundary condition type (a free boundary: zero Neumann boundary condition along the edges), which is used, for example, when a surface has a prescribed heat flux, such as a perfect insulator. This boundary is stated as $\partial_v\Phi|_{\partial\Omega} = 0$ where v is the unit outward normal vector to the boundary $\partial\Omega$. For applying the boundary conditions on the inner torus surface, the Dirichlet condition should be employed.

For further achievements, the definition of Laplacian on a Riemannian manifold as well as the FEM is required. The weak form of Navier's equation is provided in Supplementary Materials (D). From the expression of ∇_g and div_g in local coordinates, (x_1, x_2, \dots, x_n) it is straightforward to write the Laplacian in local coordinates as [77]:

$$\Delta_g = -\frac{1}{\sqrt{|\det g|}} \sum_{ij=1}^n \frac{\partial}{\partial x_i} \left(g^{ij} \sqrt{|\det g|} \frac{\partial}{\partial x_j} \right) \quad (79)$$

where g is a Riemannian metric on a manifold defined thoroughly $g = \begin{bmatrix} (R + r \cos(\phi))^2 & 0 \\ 0 & r^2 \end{bmatrix}$. A mapping transformation is determined to transform the surface of the torus to a square by creating a gluing both pairs of opposite edges together with no twists to represent how the coordinates u and v map on to the torus [78] (Fig. 13). This Figure demonstrates a gluing diagram for the torus. To understand this, first imagine bringing two of the edges together to form a cylinder (without top and bottom, just the sides of a tin can). Because the circle at the top of the can and the circle at the bottom of the can are to be glued together, we can imagine stretching the can around and gluing them to obtain a surface that looks like the surface of a donut. First, we parametrize the surface of the torus employing the same coordinates on the surface of the torus considering $X = 0$ with $X = a$ (and $Y = 0$ with $Y = b$), respectively. This is to map a point on the torus in 3D onto the square of width a and height b . Hence, any arbitrary point P on the square has the coordinates (X, Y) with $0 \leq X \leq a$ and $0 \leq Y \leq b$. For the torus centered on $O = (0, 0, 0)$ one possible parametrization of the surface is given by $((R + r \cos(v)) \cos u, (R + r \cos(v)) \sin u, r \sin v)$, where R is the radius of the torus and r is the radius of the tube. Here, the map read $u \leftrightarrow \frac{2\pi X}{a}$ and $v \leftrightarrow \frac{2\pi Y}{b}$ such the procedure we can do with a square by first rolling it to a cylinder and then connecting the ends of the cylinder. The mapping (morphing a torus into a square) must be such that each tiny square ds on the square must transform to something non-square on the surface of the torus. If we want to have a repeatable square domain (right image in Fig. 13), it should be cut using a torus. Now we define quotient space in the domain $\left[0, 0\right], \left\{\frac{2\pi}{a}, \frac{2\pi}{b}\right\}$.

The periodic boundary conditions are considered to treat the wave equation. The periodic boundary condition allows connecting the two edges of the gluing diagram. This can be imagined by creating a large square grid where the partial differential equation solution repeats itself in each square. By applying the initial bump (impact to an object) at points $\left\{u = \frac{\pi}{2}, v = \frac{\pi}{2}\right\}$ and using FEM, wave equation $(\nabla^2\Phi = \zeta \frac{\partial^2\Phi}{\partial t^2})$ can be solved. Flowchart for the theoretical formulation and solutions are provided in Supplementary Materials (E). To define the initial condition, it should be noted that it is necessary to have a function that lies on the surface of the torus. The function seems to be a real-valued function of pair variables $\{u, v\}$. The parametric form for the torus is considered $\{\cos u(R + r \cos(v)), \sin u(R + r \cos(v)), r \sin(v)\}$, $u, v \in [0, 2\pi]$. The parametric curve form of the torus can be regarded as $u = u(t)$, $v = v(t)$ to make a line on the torus. We consider a function as $u =$

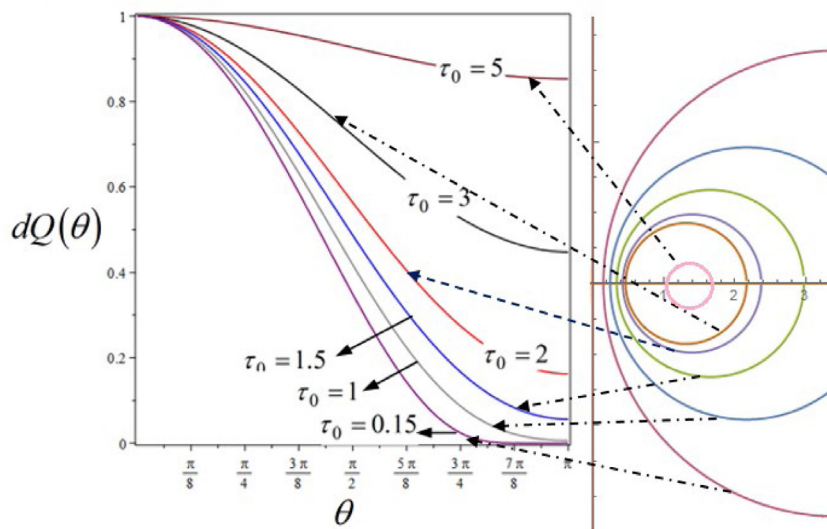


Fig. 12. Surface charge against the circle angle θ ($\Phi_0 = 10$, $R = 1$, and $N = 60$).

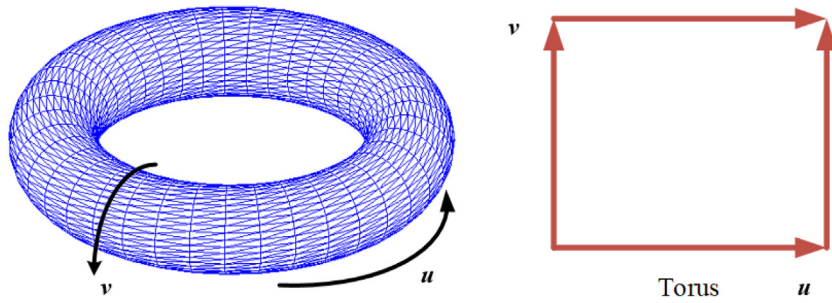


Fig. 13. Mapping the surface of a torus to a square.

$3t_0$, $v = 2t_0$, $t_0 \in [0, 2\pi]$. The initial condition considered is assumed as $\Phi(0, u, v) = e^{-(8(u-\alpha))^2 - (8(v-\beta))^2}$, $\frac{\partial \Phi}{\partial t}(0, u, v) = 0$. For the boundary condition, the Dirichlet type read $\Phi(\pi, v) = \Phi(u, \pi) = 0$. In Figs. 14–16, particular numerical solutions to the wave equation on a torus where the value of the solution is displayed using a gradient. This model considers the metric and topology of the torus.

5.5. Treating vector potential on the micro-torus surface

As stated before, the second equation in Navier's equation is $\nabla^2\Psi - (\mu/2)^2 \nabla^4\Psi - \frac{\rho}{c} \ddot{\Psi} = 0$ which contains the length scale parameter. The solution of Eq. (80) releases Figs. 17 and 18. The assumed boundary and initial conditions are:

$$\begin{aligned}\Psi(t, 0, v) &= \Psi(t, 2\pi, v), \Psi(t, u, 0) = \Psi(t, u, 2\pi), \\ \Psi(0, u, v) &= e^{-(2(u-\pi))^2 - (2(v-\pi))^2}, \frac{\partial \Psi}{\partial t}(0, u, v) = 0\end{aligned}\quad (80)$$

Figs. 17 and 18 present the solution of Navier's equation obtained for function Ψ for micro-torus made of [110] direction silicon [79] and gold [80], respectively. The material properties of silicon with the direction [110] $\mu = 0.592 \text{ }\mu\text{m}$, $E = 169 \text{ GPa}$, $\rho = 2332 \frac{\text{kg}}{\text{m}^3}$, and $\nu = 0.3$ moreover for gold are $E = 79 \text{ GPa}$, $\rho = 19300 \frac{\text{kg}}{\text{m}^3}$, $\mu = 0.47 \text{ }\mu\text{m}$, and $\nu = 0.43$. Furthermore, the time changes from zero to one second.

5.6. Discussion on eigenmodes of a micro-torus

To extract the eigenmodes of a microstructure, the formulation presented in the previous paper by the authors [4] is employed. The corresponding 3D PDE wave equation for a linear elastic material based on MCST is Eq. (23).

5.6.1. Special case: Discussion on the eigenmodes of a cylindrical micro-shell

The considered micro-cylinder is made of gold with material properties $\mu = 0.47 \text{ }\mu\text{m}$, $E = 79 \text{ GPa}$, $\nu = 0.43$, $\rho = 19300 \frac{\text{kg}}{\text{m}^3}$ [80]. The assumed geometry of the micro cylinder is $0.6 \leq X^2 + Y^2 \leq 1$, $0 \leq Z \leq 4$. Dirichlet boundary condition type is applied at the clamped end of the cylinder, i.e., $U(X, Y, 0) = 0$ (the bottom of the cylinder is clamped). Fig. 19 demonstrates the first twelve eigenvalues (GHz), and the corresponding visualized modal shapes. Fig. 20 illustrates the 3D elastic waves in a micro-cylindrical shell made of silicon with the direction [110] assuming $6.94119 \times 10^{-4} \leq X^2 + Y^2 \leq 1.0462 \times 10^{-3}$, $0 \leq Z \leq 0.14$. The silicon [79] properties are $\mu = 0.592 \text{ }\mu\text{m}$, $E = 169 \text{ GPa}$, $\rho = 2332 \frac{\text{kg}}{\text{m}^3}$, and $\nu = 0.3$. The corresponding 3D mode shapes U , V , and W for a specific frequency are presented. It should be noted that the color contours illustrate the displacements. The eigenfrequencies f_k are derived from the circular frequencies ω_k , as $f_k = \frac{\omega_k}{2\pi}$.

5.6.2. Micro-torus

Tori are a surface of the revolution created by revolving a circle about an axis coplanar with the circle in a 3D space of Euclidean geometry. In Cartesian coordinates, the implicit equation of a torus

radially symmetric about the Z -axis is: $(C - \sqrt{X^2 + Y^2})^2 + Z^2 = 0.95A^2$, where C , the major radius is the distance between the center of the hole and the center of the tube, while A , called the minor radius, is the radius of the tube (see Fig. 1)). Figs. 21, and 22 depict the 3D elastic waves and the associated eigenvalues for two different geometry micro-torus made of [110]-direction silicon [79], with material properties $\mu = 0.592 \text{ }\mu\text{m}$, $E = 169 \text{ GPa}$, $\rho = 2332 \frac{\text{kg}}{\text{m}^3}$, $\nu = 0.3$. The natural frequencies are in Hertz. It should be noted that Fig. 22 needs to constrain the ends of micro tours. Here DirichletCondition is used at $Z = 0$.

5.7. Biharmonic equation in toroidal coordinates

On the curved surfaces, the Laplacian is replaced by the Laplace-Beltrami operator [66]:

$$\bar{\nabla}^2 = \frac{1}{\sqrt{g}} \partial_i \sqrt{g} g^{ij} \partial_j \quad (81)$$

Higher powers of the Laplace Beltrami operator, particularly in relation to the Biharmonic operator on a curved space, can be stated as $\bar{\nabla}^4\Psi = \bar{\nabla}^2(\bar{\nabla}^2\Psi)$. Any solution for the Laplace equation is also a solution for the biharmonic equation, but the reverse statement is not generally true. Therefore, we assume a more general solution for the biharmonic equation (Eq. (11)). Taking a separated variable form similar to the harmonic case alongside the exponentials forms for σ , ϕ and leaving τ to be undetermined, i.e. $\Psi = \sqrt{\cosh(\tau) - \cos(\sigma)} e^{in\sigma} e^{im\phi} f(\tau)$. Accordingly, the following equation is a second-order ODE for $T(\tau)$ reducible to Legendre's equation because the dependency on σ and ϕ is eliminated ((See Supplementary Materials C; Eq. [C.11-C.15])). In the biharmonic case, by considering $\Psi = \sqrt{\cosh(\tau) - \cos(\sigma)} e^{in\sigma} e^{im\phi} f(\tau)$ and plugging it into the biharmonic equation ($\bar{\nabla}^4\Psi$), the resulting equation should be factorized if a fourth-order ODE is obtained. Each class of solution function is a harmonic, and the other is the product of toroidal harmonics [81]. If the factors are both the same, an inhomogeneous ODE with Legendre functions on the right-hand side is obtained for the functions that are biharmonic but not harmonic (See Supplementary Materials C). Solutions of the biharmonic equation in toroidal coordinates can also be given in terms of toroidal harmonics. They can be obtained by observing that if Ψ is the solution of $\bar{\nabla}^2\Psi = 0$, then Ψ , $X\Psi$, $Y\Psi$, $Z\Psi$ and $(X^2 + Y^2 + Z^2)\Psi$ are all the solutions for $\bar{\nabla}^4\Psi = 0$. In this way, one can show that the general periodic solution of the homogeneous biharmonic equation in toroidal coordinates read as:

$$\begin{aligned}\Psi &= \sinh(\tau) \sum_{m=0}^{\infty} \sum_{n=1}^{\infty} [A_{nm} T_{n+1,m} + B_{nm} T_{n-1,m} + C_{nm} S_{n+1,m} + D_{nm} S_{n-1,m}] \begin{cases} \cos n\sigma \\ \sin n\sigma \end{cases} \times \begin{cases} \cos m\phi \\ \sin m\phi \end{cases} \\ &+ \frac{\sinh(\tau)}{\sqrt{\cosh(\tau) - \cos(\sigma)}} \sum_{n=0}^{\infty} [A_{n1} T_{n+1,1} + B_{n1} T_{n-1,1} + C_{n1} S_{n+1,1} + D_{n1} S_{n-1,1}] \begin{cases} \cos n\sigma \\ \sin n\sigma \end{cases} \end{aligned}\quad (82)$$

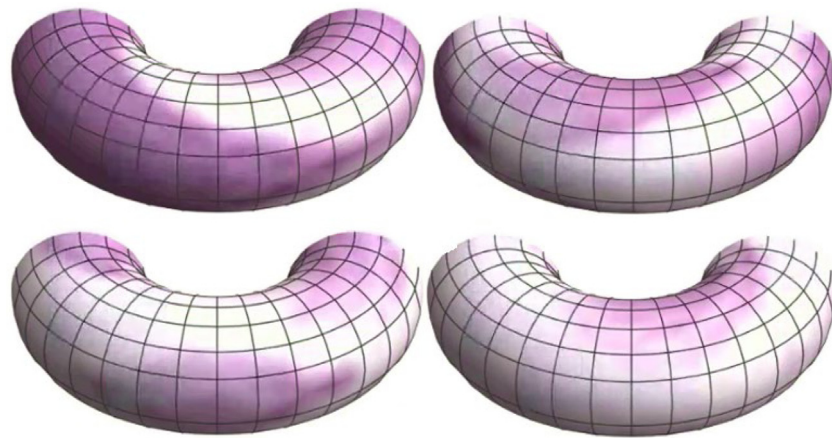


Fig. 14. Wave propagation in a micro torus with $R = 2, r = 1, \alpha = \beta = \pi, \zeta = 0.5$, and $a = b = 1$.

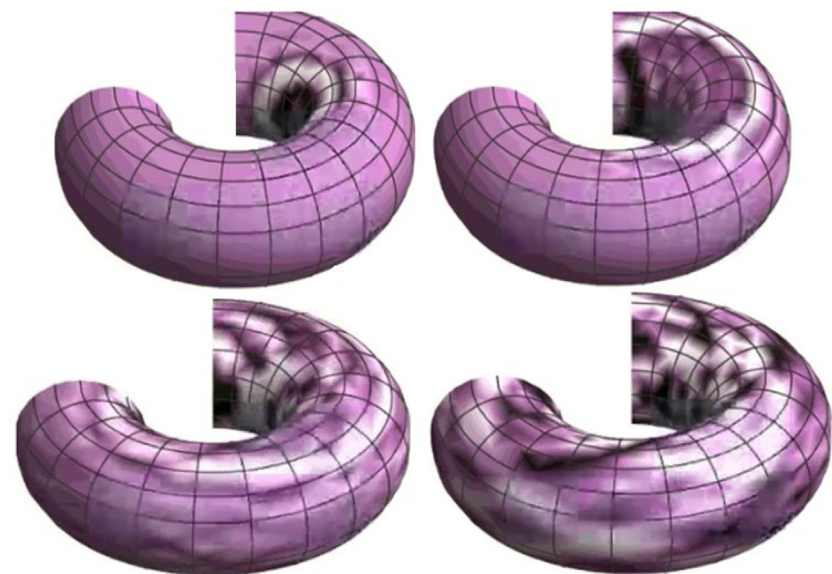


Fig. 15. Wave propagation in a micro torus with $R = 2, r = 1, \alpha = \beta = \pi, \zeta = 0.5$, and $a = b = 1$.

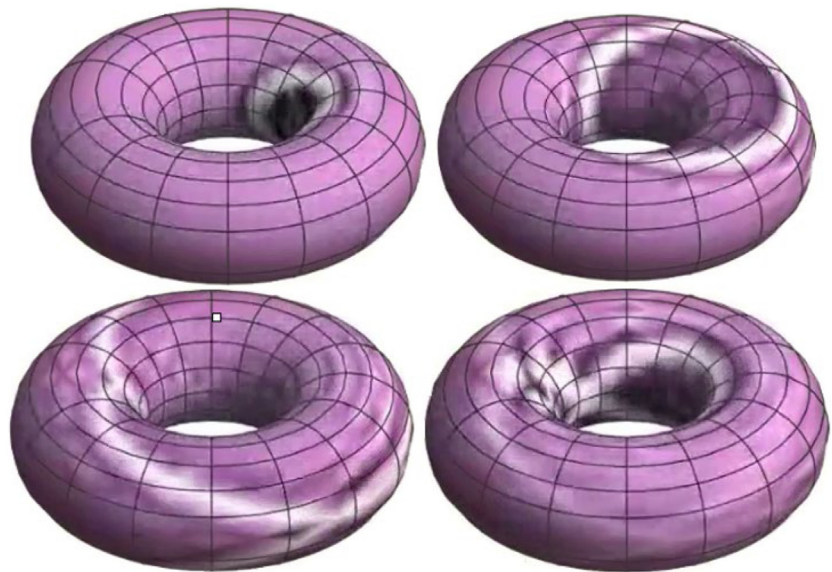


Fig. 16. Wave propagation in a micro-torus with $R = 2, r = 1, \alpha = \beta = \pi, \zeta = 0.5$, and $a = b = 1$.

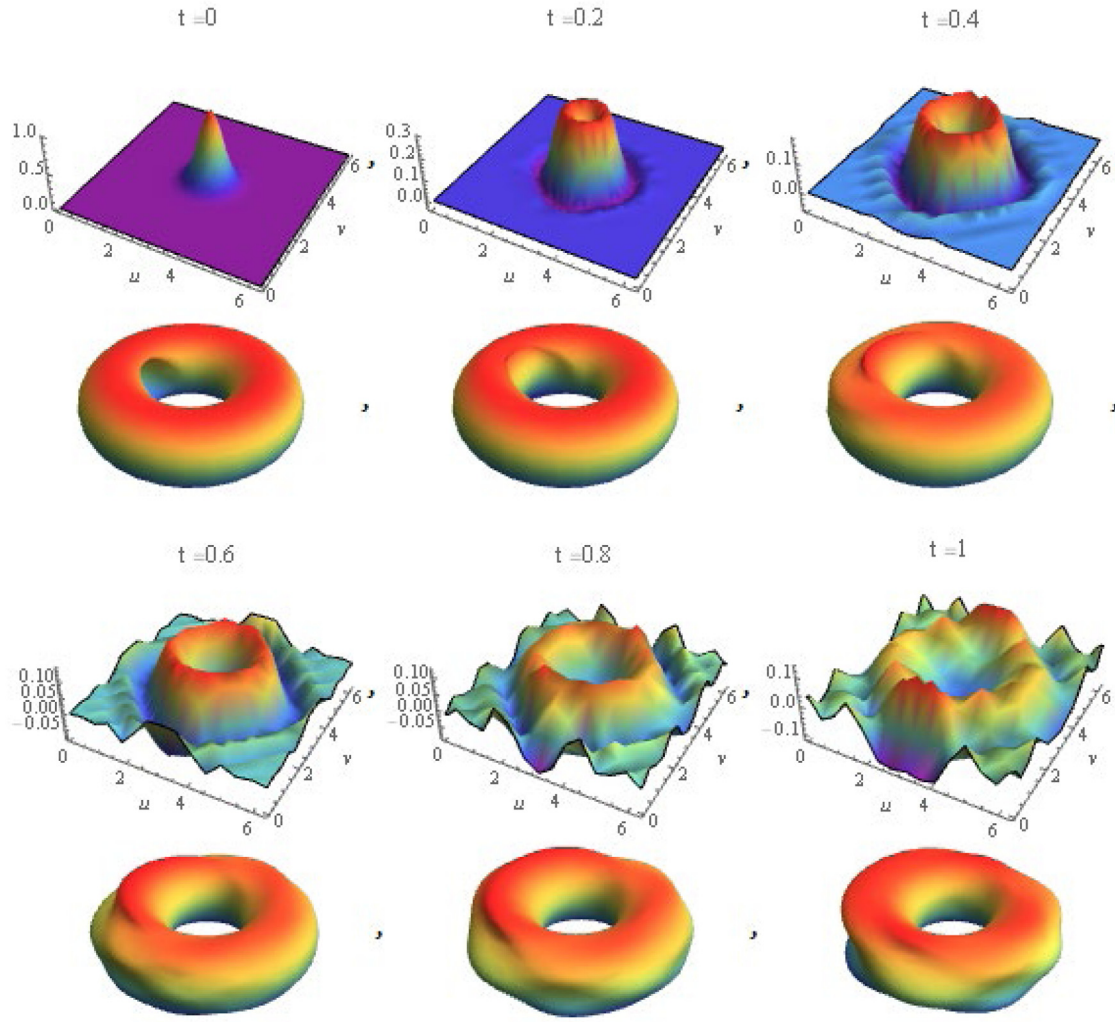


Fig. 17. Visualization of potential Ψ on the surface of a micro torus made of silicon with the direction [110].

where $T_{nm}(\tau) \equiv Q_{n-1/2}^m(\cosh(\tau))$, $S_{nm}(\tau) \equiv P_{n-1/2}^m(\cosh(\tau))$ and A_{nm} , B_{nm} , C_{nm} , D_{nm} are arbitrary constants. We also have the continuity conditions $\Psi_{\sigma=-\pi} = \Psi_{\sigma=\pi}$, $\frac{\partial \Psi}{\partial \sigma} \Big|_{\sigma=-\pi} = \frac{\partial \Psi}{\partial \sigma} \Big|_{\sigma=\pi}$, which are equivalent to the physical requirement that the solutions must be periodic in the “cyclic” coordinate σ . The above conditions are possible only if the parameter n is an integer number. Furthermore, without loss of generality, we can assume that it is a non-negative number.

5.7.1. Treating the Laplace equation on a torus

The six smallest eigenvalues and eigenfunctions of the Laplace equation on a square torus (considering periodic boundary conditions on a square of length 2) with a Dirichlet constraint are shown in Fig. 23. Dirichlet boundary condition type is regarded as $U[X, Y] = 0|_{X=Y=0}$. The corresponding non-dimensional eigenvalues are $\{0.347, 9.870, 9.870, 11.308, 19.740, 21.536\}$. As seen, the first eigenfunction has only one nodal domain, while the other eigenfunctions have more nodal domains. An increase of the mode number leads to stronger localization of the eigenfunction near the boundary.

5.7.2. Extracting the eigenfunctions of a 3D Laplacian on a torus

The first six eigenfunctions of the Laplacian operator on the free torus structure, which has the following geometry $\left(\sqrt{(X^2 + Y^2)} - 0.9\right)^2 + Z^2 \leq 0.1$, are presented in Fig. 24. The associated non-dimensional eigenvalues are $\{0, 1.269, 1.270, 5.008, 5.009, 11.023\}$. As can be seen,

the first/sixth eigenfunctions are symmetric eigenmodes and are not complex eigenmodes.

5.8. Treating the Helmholtz equation via FEM

The description of many properties of nano/microsystems in the framework of a continuous-medium approximation requires the solution of the Helmholtz equation. Here the FEM is employed to find the corresponding eigenvalues and eigenfunctions of the PDE operator over a given toroidal domain. From Eq. (24), with an assumed harmonic time dependency $\Phi = \phi e^{\pm i\omega t}$, the Helmholtz equation with Dirichlet boundary conditions read $\nabla^2 \phi(\sigma, \tau, \phi) + \varsigma^2 \phi(\sigma, \tau, \phi) = 0$, $(\sigma, \tau, \phi) \in \Omega$, $\phi(\sigma, \tau, \phi) = 0$, $(\sigma, \tau, \phi) \in \partial\Omega$ where $\phi_\varsigma = e^{im\phi}$, $|m| = \varsigma$. ς indicates the potential parameter (wave number) and Ω is the 3D toroidal boundary. The Laplace or Laplace-Beltrami operators are independent relative to a selected coordinate system [82]. However, the existence of the solution depends on the global geometry of the manifold on which the solution is requested. In specific, it is related to the spectrum of the Laplace-Beltrami operator. For $r_c/R \rightarrow \infty$, the torus tends towards a circular cylinder. The major torus circumference becomes the cylinder axis of revolution. The toroid section by an axial plane tends to the section of the cylinder by a plane normal to the cylinder axis. This leads to solving the Helmholtz equation in a different set of cylindrical coordinates.

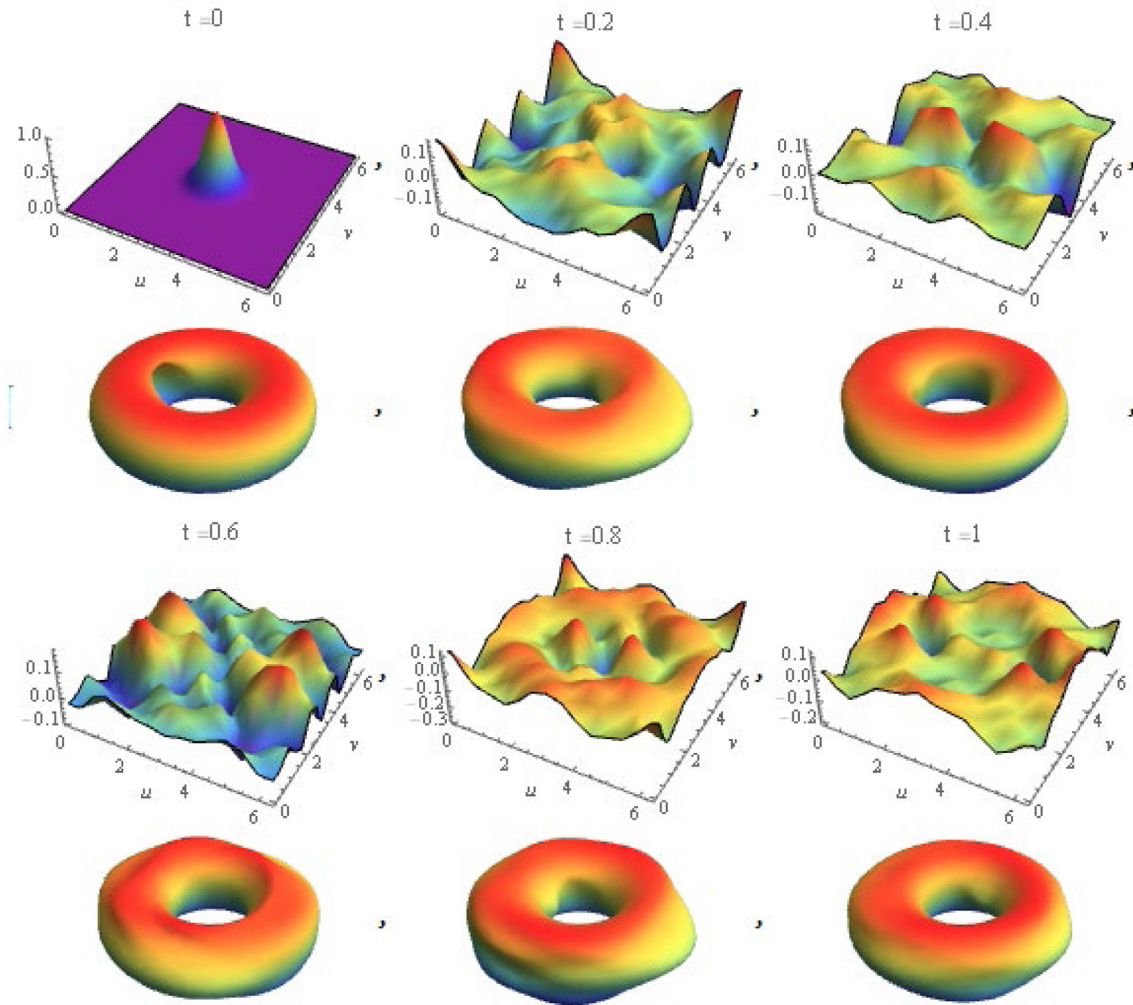


Fig. 18. Visualization of potential Ψ on the surface of a micro torus made of gold.

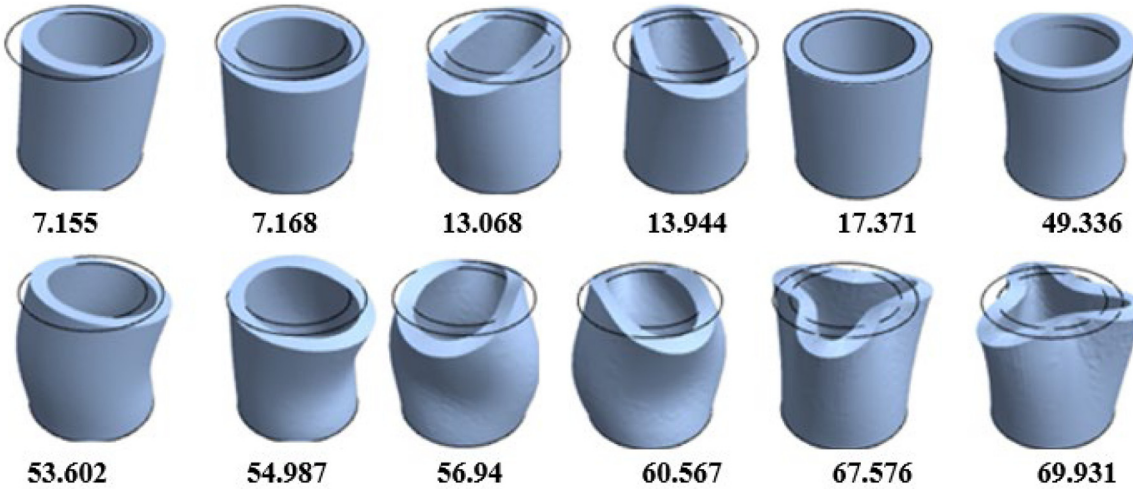


Fig. 19. Visualization of mode shapes of the micro-cylindrical shell and the corresponding eigenvalues (GHz).

Contrary to the case of tori, the Helmholtz equation separates for cylinders. Fig. 25 demonstrates the solution of the Helmholtz equation, i.e. $\nabla^2\phi(\sigma, \tau, \phi) + \zeta^2\phi(\sigma, \tau, \phi) = 0$, for the cylindrical structure. Fig. 26

presents the results for a torus structure $\left(\sqrt{(X^2 + Y^2)} - 0.9\right)^2 + Z^2 \leq 0.1$ considering the Dirichlet boundary condition $U(X, Y, Z) = 0$.

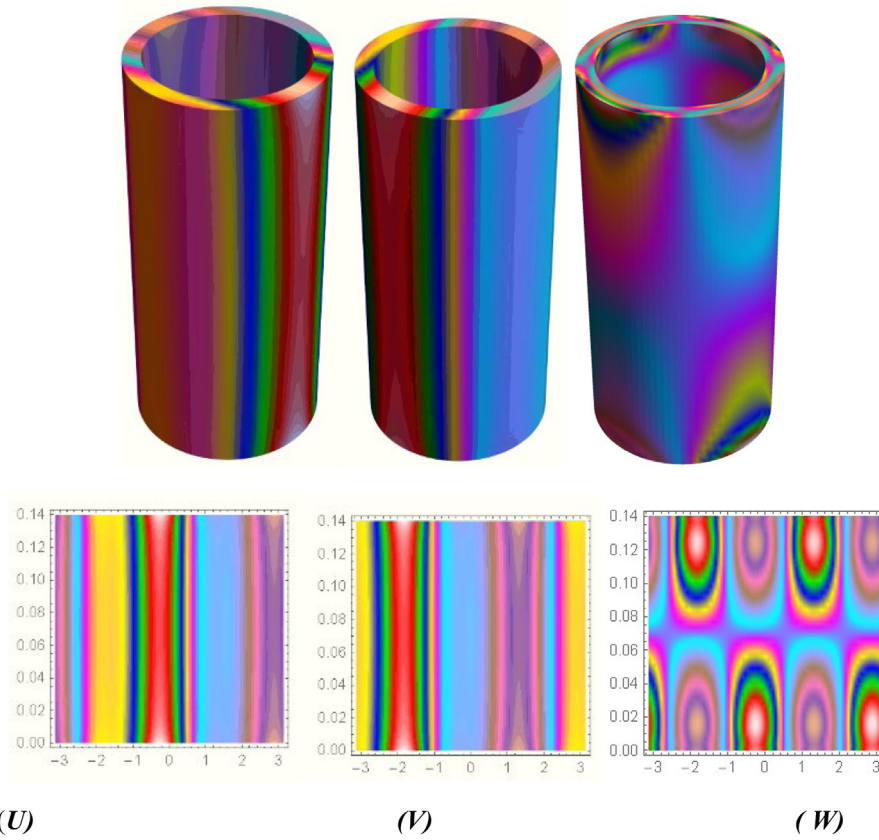


Fig. 20. 3D elastic waves in a micro-cylindrical shell made of silicon with the direction [110]; ($f = 7688.6$ [Hz]).

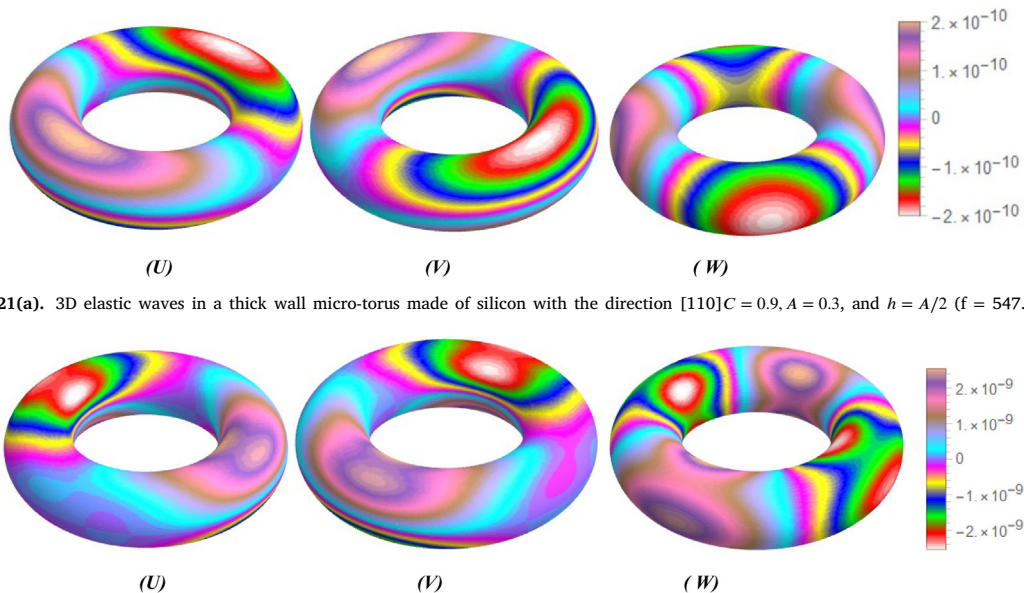


Fig. 21(a). 3D elastic waves in a thick wall micro-torus made of silicon with the direction $[110]C = 0.9$, $A = 0.3$, and $h = A/2$ ($f = 547.337$).

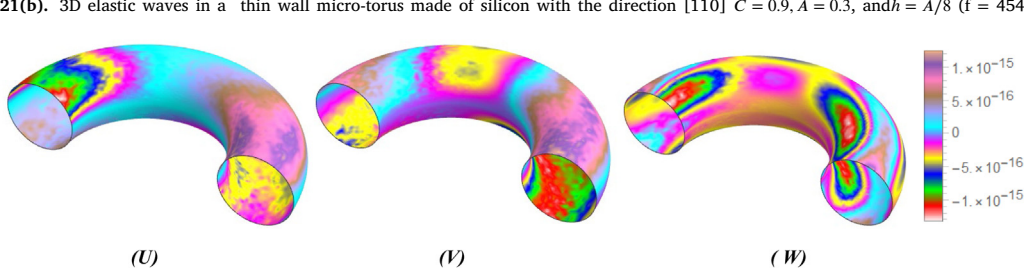


Fig. 22(a). 3D elastic waves in a thick micro-torus made of silicon with the direction [110] $C = 0.9$, $A = 0.3$, and $h = A/4$ ($f = 1875.28$).

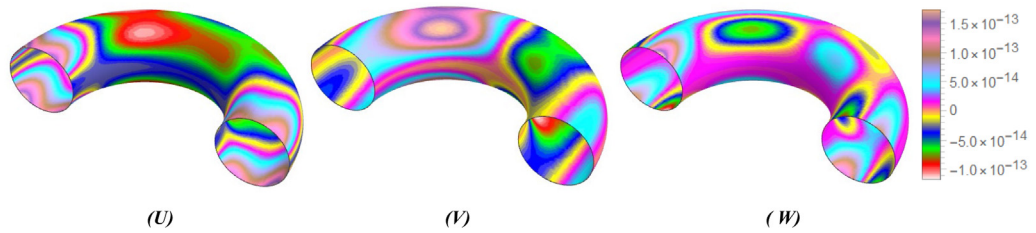


Fig. 22(b). 3D elastic waves in a thin micro-torus made of silicon with the direction [110] $C = 0.9$, $A = 0.3$, and $h = A/8$ ($f = 1552.18$).

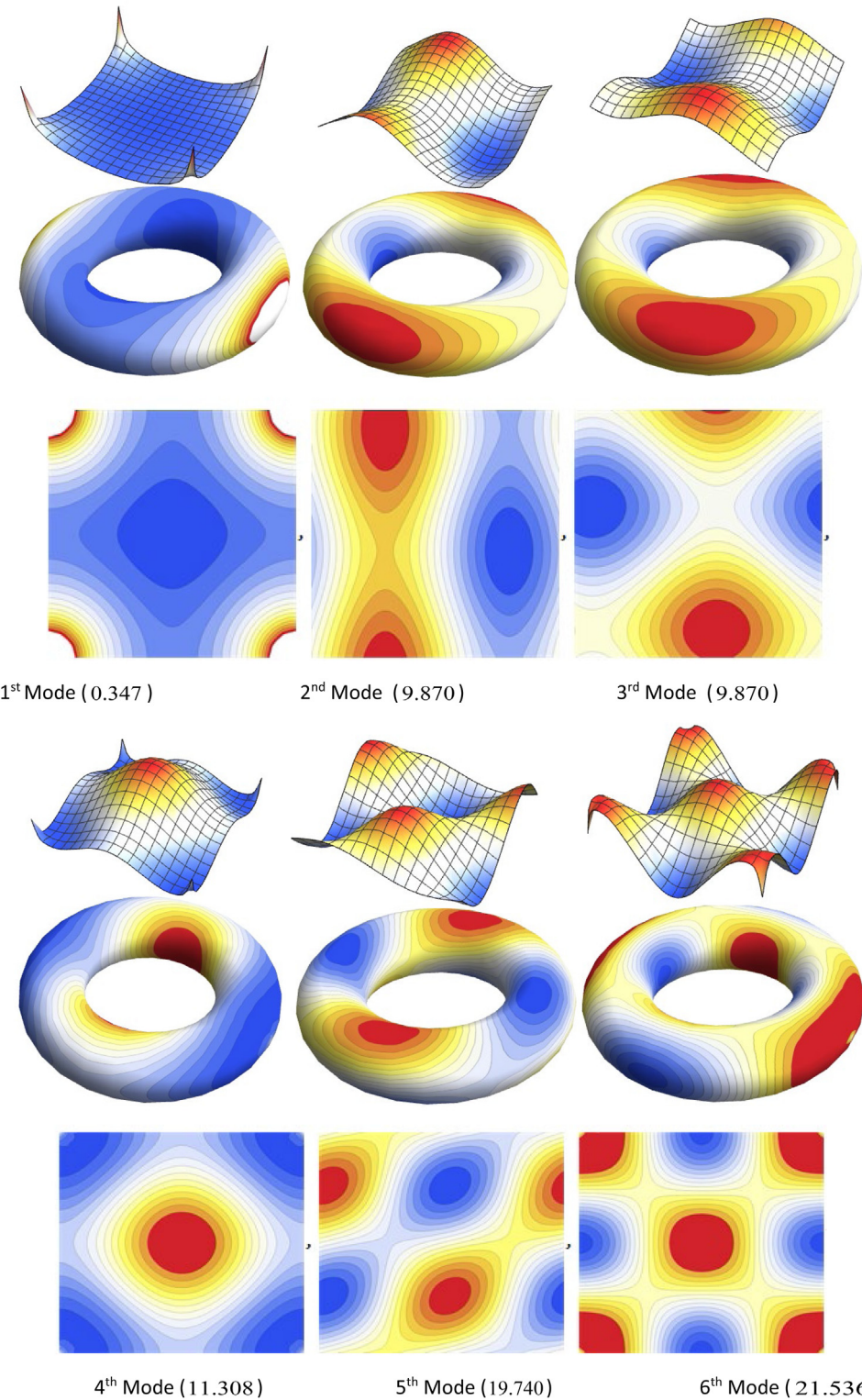


Fig. 23. Eigenfunctions of a Laplace equation on a torus (considering periodic boundary conditions on a square with the length of 2) with a Dirichlet constraint.

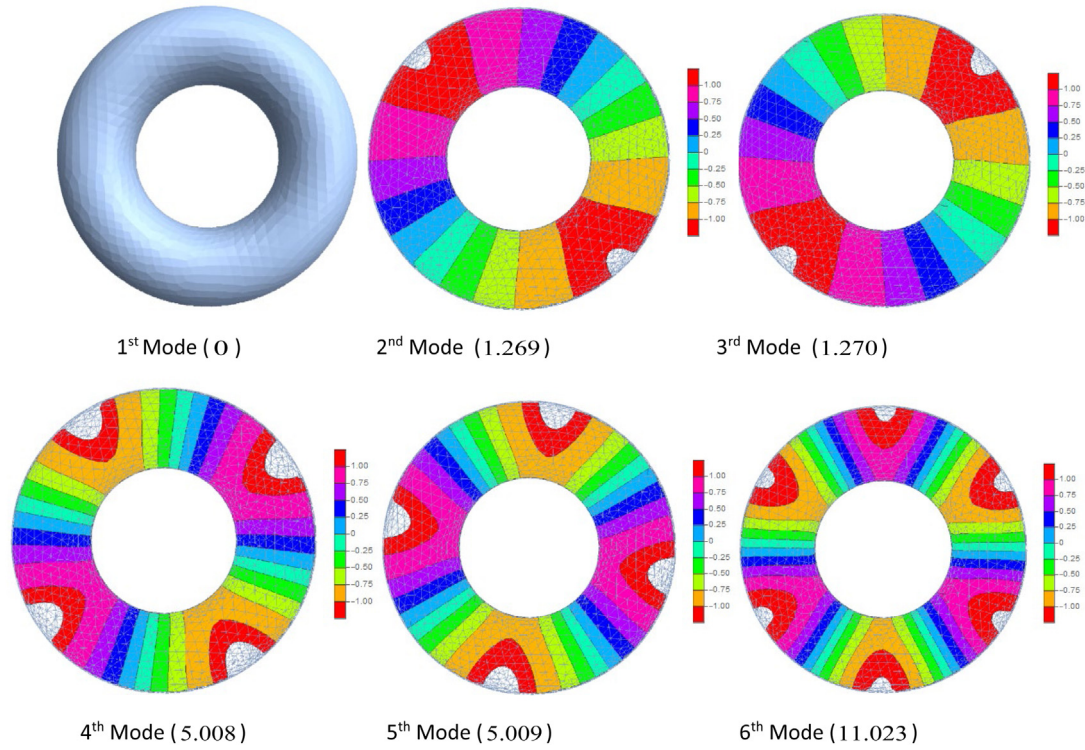


Fig. 24. Visualization of the first six eigenfunctions of the Laplacian operator on the torus structure.

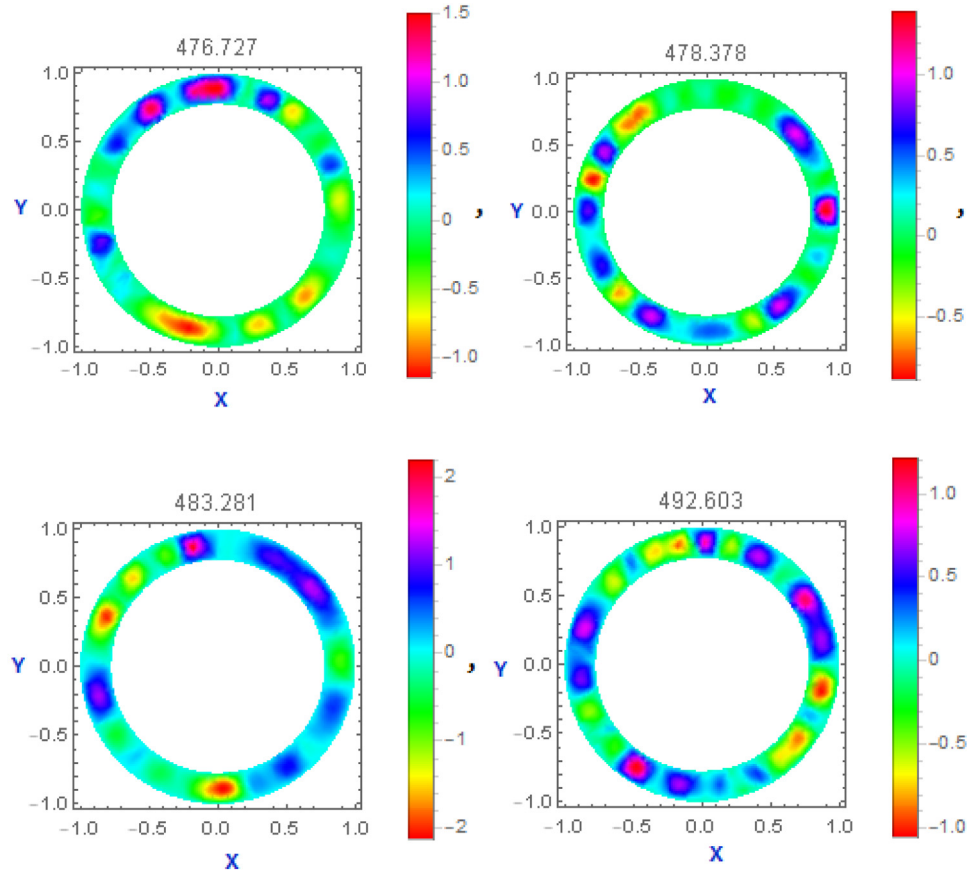


Fig. 25. The solution of the Helmholtz equation for cylindrical structure as $0.6 \leq X^2 + Y^2 \leq 1, 0 \leq Z \leq 4$ by considering Dirichlet boundary condition $U(X, Y, Z) = 0$, and $\zeta = 1$.

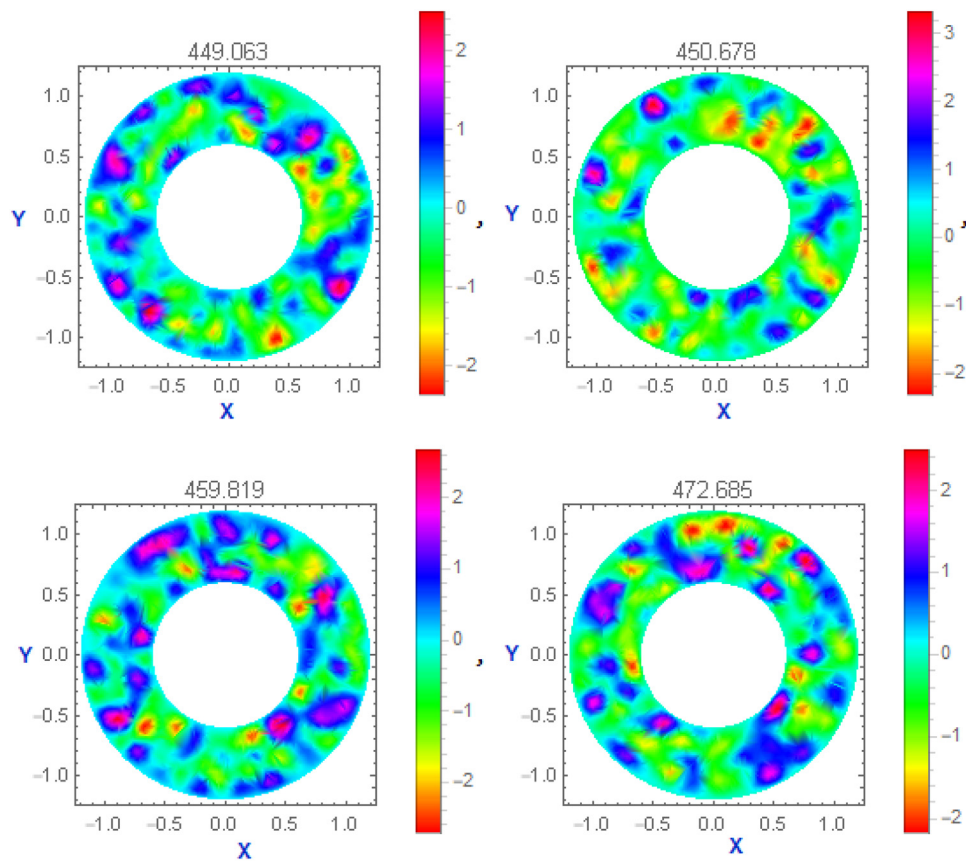


Fig. 26. The solution of the Helmholtz equation for a torus structure $\left(\sqrt{(X^2 + Y^2)} - 0.9\right)^2 + Z^2 \leq 0.1$ considering the Dirichlet boundary condition $U(X, Y, Z) = 0$, and $\zeta = 1$.

6. Concluding remarks

The free vibration and dynamic wave propagation of micro-torus structures through MCST based on 3D constitutive elasticity relations were discussed in this paper. Traditional theories of elasticity fail to account for the size effects in the micro-structures. Consequently, their outcomes are inaccurate enough to be non-reliable in the sub-size structures. To circumvent such dilemmas, resorting to a non-classical continuum theory capable of capturing the size effect is inevitable. A mathematical formulation was developed in the toroidal coordinates in the form of Navier's equations in the framework of modified couple stress theory. Navier's equations in toroidal coordinates were decomposed through the Helmholtz equation into Laplacian and biharmonic ones to study the potential charge distribution in conducting micro-torus structures. Several micro-torus problems were solved numerically by the finite element method (FEM) to find eigenvalues and eigenfunctions from the elastic wave propagation standpoints. There are numerous applications of Laplacian eigenfunctions. For instance, Laplacian eigenfunctions can be used to investigate the increased damping in irregular acoustics cavities. Using the eigenfunctions of the Laplace operator, one can analyze and represent data recorded on general domains. For the first time in the open literature, a complete calculation for finding Divergence, Laplacian operator, Laplacian of Laplacian, Gradient, Curl, the divergence of the second-order tensors, the gradient of the divergence for the vector fields, and an arbitrary general scalar function was developed in the toroidal coordinates. The current study revealed that:

- The length scale parameter considered in the MCST is essential for quantitative estimation of the wave propagation analysis in high-frequency ranges, damage detection, and cut-off frequencies.

- The wave propagation characteristics in the torus structures demonstrate how the elastic waves are affected by the micro-tours curvature.
- The Rayleigh-Ritz method results are consistent with other natural frequencies obtained by other findings of researchers (Table 1).
- The Laplacian operator of the first/sixth torus eigenfunctions is not complex and symmetric eigenmodes (Fig. 24).
- For a thinner torus (larger τ_0), the potential drops more in the toroid center (Fig. 4).
- In the case of surface charge density, as the tori get fatter, the dQ distribution becomes more peaked at $\theta = 0$. The peak value for dQ occurs on the outside equator ($\theta = 0$) (Fig. 12).
- Frequency localization is important first for the theory of Laplacian eigenproblems and second, from a practical point of view, for the theory of acoustics and quantum waveguides.
- Treating the Laplace equation on a torus helps to prove more precisely the frequency localization of Laplacian eigenfunctions, i.e., how an eigenfunction is getting distributed in a small region of the domain and decays rapidly outside this region.
- The main disadvantage of the use of toroidal harmonics is the presence of associated Legendre functions with half-integer indexes, whose trend is problematic to evaluate.

CRediT authorship contribution statement

I. Karimipour: Methodology, Software, Validation, Formal analysis, Writing - original draft, Visualization. **Y. Tadi Beni:** Conceptualization, Resources, Methodology, Software, Validation, Formal analysis, Investigation, Data curation, Writing - review & editing, Visualization, Supervision, Project administration. **Hadi Arvin:** Conceptualization,

Resources, Writing - review & editing, Visualization, Supervision. A.H. Akbarzadeh: Conceptualization, Resources, Data curation, Writing - review & editing, Visualization, Supervision, Project administration.

Declaration of competing interest

The authors declare that they have no known competing financial interests or personal relationships that could have appeared to influence the work reported in this paper.

Appendix A. Supplementary data

Supplementary material related to this article can be found online at <https://doi.org/10.1016/j.tws.2021.107995>. Supplementary data to this article can be found online.

References

- [1] X.W. Gu, C.N. Loynachan, Z. Wu, Y.-W. Zhang, D.J. Srolovitz, J.R. Greer, Size-dependent deformation of nanocrystalline Pt nanopillars, *Nano Lett.* 12 (2012) 6385–6392.
- [2] F. Zhang, D. Redekop, Surface loading of a thin-walled toroidal shell, *Comput. Struct.* 43 (1992) 1019–1028.
- [3] M. Abbasipour, R. Khajavi, A.A. Yousefi, M.E. Yazdanshenas, F. Razaghian, A. Akbarzadeh, Improving piezoelectric and pyroelectric properties of electrospun PVDF nanofibers using nanofillers for energy harvesting application, *Polym. Adv. Technol.* 30 (2019) 279–291.
- [4] I. Karimipour, Y. Tadi Beni, A.H. Akbarzadeh, Modified couple stress theory for three-dimensional elasticity in curvilinear coordinate system: application to micro torus panels, *Mechanica* (2020) <http://dx.doi.org/10.1007/s11012-020-01220-3>.
- [5] J. Blachut, O.R. Jaiswal, On buckling of toroidal shells under external pressure, *Comput. Struct.* 77 (2000) 233–251.
- [6] P.-T. Thang, T. Nguyen-Thoi, A new approach for non-linear dynamic buckling of S-FGM toroidal shell segments with axial and circumferential stiffeners, *Aerospace Sci. Technol.* 53 (2016) 1–9.
- [7] D. Redekop, X.H. Wang, Free vibration of a magneto-electro-elastic toroidal shell, in: *Comput. Civ. Build. Eng. Proc. Int. Conf.*, 2010, p. 505.
- [8] G.R. Buchanan, Y.J. Liu, An analysis of the free vibration of thick-walled isotropic toroidal shells, *Int. J. Mech. Sci.* 47 (2005) 277–292.
- [9] H.S. Tzou, D.W. Wang, Vibration control of toroidal shells with parallel and diagonal piezoelectric actuators, *J. Press. Vessel Technol.* 125 (2003) 171–176.
- [10] J.-H. Kang, Vibration analysis of toroidal shells with hollow circular cross-section having variable thickness, *J. Eng. Mech.* 142 (2016) 4016058.
- [11] H.Y. Sarvestani, S.V. Hoa, M. Hojjati, Three-dimensional stress analysis of orthotropic curved tubes-part 1: single-layer solution, *Eur. J. Mech. A* 60 (2016) 327–338.
- [12] J. Morsbøl, S.V. Sorokin, Elastic wave propagation in curved flexible pipes, *Int. J. Solids Struct.* 75–76 (2015) 143–155, <http://dx.doi.org/10.1016/j.ijsolstr.2015.08.009>.
- [13] E.B. Groth, T.G.R. Clarke, G. da Silva, I. Iturrioz, G. Lacidogna, The elastic wave propagation in rectangular waveguide structure: Determination of dispersion curves and their application in nondestructive techniques, *Appl. Sci.* 10 (2020) 4401.
- [14] J. Yu, J.E. Lefebvre, L. Elmaimouni, Toroidal wave in multilayered spherical curved plates, *J. Sound Vib.* 332 (2013) 2816–2830, <http://dx.doi.org/10.1016/j.jsv.2012.12.032>.
- [15] H. Darban, F. Fabbrocino, R. Luciano, Size-dependent linear elastic fracture of nanobeams, *Internat. J. Engrg. Sci.* 157 (2020) 103381.
- [16] O. Rahmani, O. Pedram, Analysis and modeling the size effect on vibration of functionally graded nanobeams based on nonlocal Timoshenko beam theory, *Internat. J. Engrg. Sci.* 77 (2014) 55–70, <http://dx.doi.org/10.1016/j.ijengsci.2013.12.003>.
- [17] H.M. Ma, X.-L. Gao, J.N. Reddy, A microstructure-dependent Timoshenko beam model based on a modified couple stress theory, *J. Mech. Phys. Solids* 56 (2008) 3379–3391, <http://dx.doi.org/10.1016/j.jmps.2008.09.007>.
- [18] M.Z. Nejad, A. Hadi, A. Rastgoor, Buckling analysis of arbitrary two-directional functionally graded Euler-Bernoulli nano-beams based on nonlocal elasticity theory, *Internat. J. Engrg. Sci.* 103 (2016) 1–10, <http://dx.doi.org/10.1016/j.ijengsci.2016.03.001>.
- [19] A.C. Eringen, D.G.B. Edelen, On nonlocal elasticity, *Internat. J. Engrg. Sci.* 10 (1972) 233–248, [http://dx.doi.org/10.1016/0020-7225\(72\)90039-0](http://dx.doi.org/10.1016/0020-7225(72)90039-0).
- [20] E. Cosserat, F. Cosserat, *Théorie des corps déformables*, 1909.
- [21] D.C.C. Lam, F. Yang, A.C.M. Chong, J. Wang, P. Tong, Experiments and theory in strain gradient elasticity, *J. Mech. Phys. Solids* 51 (2003) 1477–1508.
- [22] I. Karimipour, Y. Tadi Beni, A.R. Karimipour, Size-dependent non-linear pull-in instability of the clamped cylindrical thin micro-nanoshell based on the non-classical theories, *Indian J. Phys.* 93 (2019) <http://dx.doi.org/10.1007/s12648-018-1332-z>.
- [23] H. Zeighampour, Y. Tadi Beni, I. Karimipour, Material length scale and nonlocal effects on the wave propagation of composite laminated cylindrical micro/nanoshells, *Eur. Phys. J. Plus* 132 (2017) <http://dx.doi.org/10.1140/epjp/i2017-11770-7>.
- [24] H. Zeighampour, Y.T. Beni, I. Karimipour, Wave propagation in double-walled carbon nanotube conveying fluid considering slip boundary condition and shell model based on nonlocal strain gradient theory, *Microfluid. Nanofluid.* 21 (2017) <http://dx.doi.org/10.1007/s10404-017-1918-3>.
- [25] Y. Tadi Beni, I. Karimipour, M. Abadyan, Modeling the instability of electrostatic nano-bridges and nano-cantilevers using modified strain gradient theory, *Appl. Math. Model.* 39 (2015) <http://dx.doi.org/10.1016/j.apm.2014.11.011>.
- [26] I. Karimipour, Y.T. Beni, H. Zeighampour, Nonlinear size-dependent pull-in instability and stress analysis of thin plate actuator based on enhanced continuum theories including non-linear effects and surface energy, *Microsyst. Technol.* 24 (2018) <http://dx.doi.org/10.1007/s00542-017-3540-4>.
- [27] I. Karimipour, A.R. Fotuhi, Anti-plane analysis of an infinite plane with multiple cracks based on strain gradient theory, *Acta Mech.* 228 (2017) 1793–1817, <http://dx.doi.org/10.1007/s00707-016-1793-0>.
- [28] I. Karimipour, Y.T. Beni, N. Taheri, Influence of electrical double-layer dispersion forces and size dependency on pull-in instability of clamped microplate immersed in ionic liquid electrolytes, *Indian J. Phys.* 91 (2017) <http://dx.doi.org/10.1007/s12648-017-1032-0>.
- [29] H. Zeighampour, Y.T. Beni, I. Karimipour, Torsional vibration and static analysis of the cylindrical shell based on strain gradient theory, *Arab. J. Sci. Eng.* 41 (2016) <http://dx.doi.org/10.1007/s13369-015-1940-2>.
- [30] F. Fan, Y. Xu, S. Sahmani, B. Safaei, Modified couple stress-based geometrically non-linear oscillations of porous functionally graded microplates using NURBS-based isogeometric approach, *Comput. Methods Appl. Mech. Engrg.* 372 (2020) 113400, <http://dx.doi.org/10.1016/j.cma.2020.113400>.
- [31] C.-L. Thanh, L.V. Tran, T. Vu-Huu, M. Abdel-Wahab, The size-dependent thermal bending and buckling analyses of composite laminate microplate based on new modified couple stress theory and isogeometric analysis, *Comput. Methods Appl. Mech. Engrg.* 350 (2019) 337–361, <http://dx.doi.org/10.1016/j.cma.2019.02.028>.
- [32] H.X. Nguyen, T.N. Nguyen, M. Abdel-Wahab, S.P.A. Bordas, H. Nguyen-Xuan, T.P. Vo, A refined quasi-3D isogeometric analysis for functionally graded microplates based on the modified couple stress theory, *Comput. Methods Appl. Mech. Engrg.* 313 (2017) 904–940, <http://dx.doi.org/10.1016/j.cma.2016.10.002>.
- [33] C.-L. Thanh, L.V. Tran, T. Vu-Huu, H. Nguyen-Xuan, M. Abdel-Wahab, Size-dependent non-linear analysis and damping responses of FG-CNTRC micro-plates, *Comput. Methods Appl. Mech. Engrg.* 353 (2019) 253–276, <http://dx.doi.org/10.1016/j.cma.2019.05.002>.
- [34] F. Abbaspour, H. Arvin, Vibration and thermal buckling analyses of three-layered centrosymmetric piezoelectric microplates based on the modified consistent couple stress theory, *J. Vib. Control* (2020) 1077546320924273.
- [35] I. Karimipour, Y.T. Beni, A.H. Akbarzadeh, Size-dependent non-linear forced vibration and dynamic stability of electrically actuated micro-plates, *Commun. Nonlinear Sci. Numer. Simul.* 78 (2019) 104856, <http://dx.doi.org/10.1016/j.cnsns.2019.104856>.
- [36] A.M. Dehrouyeh-Semnani, H. Mostafaei, Vibration analysis of scale-dependent thin shallow microshells with arbitrary planform and boundary conditions, *Int. J. Eng. Sci.* 158 (n.d.) 103413.
- [37] I. Karimipour, Y. Tadi Beni, H. Zeighampour, Vibration and dynamic behavior of electrostatic size-dependent micro-plates, *J. Braz. Soc. Mech. Sci. Eng.* 42 (2020) <http://dx.doi.org/10.1007/s40430-020-02490-4>.
- [38] Y.T. Beni, I. Karimipour, M. Abadyan, Modeling the effect of intermolecular force on the size-dependent pull-in behavior of beam-type NEMS using modified couple stress theory, *J. Mech. Sci. Technol.* 28 (2014) <http://dx.doi.org/10.1007/s12206-014-0836-5>.
- [39] I. Karimipour, Y.T. Beni, A. Koochi, M. Abadyan, Using couple stress theory for modeling the size-dependent instability of double-sided beam-type nanoactuators in the presence of casimir force, *J. Braz. Soc. Mech. Sci. Eng.* 38 (2016) <http://dx.doi.org/10.1007/s40430-015-0385-6>.
- [40] H. Rafii-Tabar, H.M. Shodja, M. Darabi, A. Dahi, Molecular dynamics simulation of crack propagation in fcc materials containing clusters of impurities, *Mech. Mater.* 38 (2006) 243–252.
- [41] A.H. Akbarzadeh, Y. Cui, Z.T. Chen, Thermal wave: from nonlocal continuum to molecular dynamics, *RSC Adv.* 7 (2017) 13623–13636.
- [42] C. Zhang, A. Akbarzadeh, W. Kang, J. Wang, A. Mirabolghasemi, Nano-architected metamaterials: Carbon nanotube-based nanotresses, *Carbon N.Y.* 131 (2018) 38–46.
- [43] J.R. Greer, J.T.M. De Hosson, Plasticity in small-sized metallic systems: Intrinsic versus extrinsic size effect, *Prog. Mater. Sci.* 56 (2011) 654–724.
- [44] D. Jang, J.R. Greer, Transition from a strong-yet-brittle to a stronger-and-ductile state by size reduction of metallic glasses, *Nature Mater.* 9 (2010) 215–219.
- [45] R.D. Mindlin, H.F. Tiersten, Effects of couple-stresses in linear elasticity, *Arch. Ration. Mech. Anal.* 11 (1962) 415–448.
- [46] R.D. Mindlin, Micro-structure in linear elasticity, *Arch. Ration. Mech. Anal.* 16 (1964) 51–78.

- [47] A.C. Eringen, On differential equations of nonlocal elasticity and solutions of screw dislocation and surface waves, *J. Appl. Phys.* 54 (1983) 4703–4710, <http://dx.doi.org/10.1063/1.332803>.
- [48] R. Barretta, L. Feo, R. Luciano, F. Marotti de Sciarra, Application of an enhanced version of the eringen differential model to nanotechnology, *Composites B* 96 (2016) 274–280, <http://dx.doi.org/10.1016/j.compositesb.2016.04.023>.
- [49] G. Romano, R. Barretta, M. Diaco, F. Marotti de Sciarra, Constitutive boundary conditions and paradoxes in nonlocal elastic nanobeams, *Int. J. Mech. Sci.* 121 (2017) 151–156, <http://dx.doi.org/10.1016/j.ijmecsci.2016.10.036>.
- [50] J. Fernández-Sáez, R. Zaera, J.A. Loya, J.N. Reddy, Bending of Euler–Bernoulli beams using Eringen's integral formulation: A paradox resolved, *Internat. J. Engrg. Sci.* 99 (2016) 107–116, <http://dx.doi.org/10.1016/j.ijengsci.2015.10.013>.
- [51] O. Göhner, Schubspannungsverteilung im querschnitt einer schraubenfeder, *Ingenieur-Archiv* 1 (1930) 619–644.
- [52] H.A. Lang, Toroidal elastic stress fields for pressurized elbows and pipe bends, *Int. J. Press. Vessels Pip.* 15 (1984) 291–305.
- [53] D. Redekop, A displacement solution in toroidal elasticity, *Int. J. Press. Vessels Pip.* 51 (1992) 189–209.
- [54] D. Redekop, Y. Zhu, A computer program for stresses in a thick-walled 90 elbow, *Comput. Struct.* 45 (1992) 805–812.
- [55] A. Golgoon, A. Yavari, On the stress field of a non-linear elastic solid torus with a toroidal inclusion, *J. Elasticity* 128 (2017) 115–145.
- [56] T.N. Nguyen, C.H. Thai, A.-T. Luu, H. Nguyen-Xuan, J. Lee, NURBS-based post-buckling analysis of functionally graded carbon nanotube-reinforced composite shells, *Comput. Methods Appl. Mech. Engrg.* 347 (2019) 983–1003.
- [57] T.N. Nguyen, T.D. Ngo, H. Nguyen-Xuan, A novel three-variable shear deformation plate formulation: theory and Isogeometric implementation, *Comput. Methods Appl. Mech. Engrg.* 326 (2017) 376–401.
- [58] C.H. Thai, S. Kulasegaram, L.V. Tran, H. Nguyen-Xuan, Generalized shear deformation theory for functionally graded isotropic and sandwich plates based on isogeometric approach, *Comput. Struct.* 141 (2014) 94–112.
- [59] H. Karami, M. Farid, A new formulation to study in-plane vibration of curved carbon nanotubes conveying viscous fluid, *J. Vib. Control* 21 (2015) 2360–2371.
- [60] H.Y. Sarvestani, Buckling analysis of curved nanotube structures based on the nonlocal shell theory, *Int. J. Multiscale Comput. Eng.* 14 (2016).
- [61] C.Y. Wang, J. Zhang, Y.Q. Fei, T. Murmu, Circumferential nonlocal effect on vibrating nanotubules, *Int. J. Mech. Sci.* 58 (2012) 86–90.
- [62] P. Soltani, A. Kassaei, M.M. Taherian, Non-linear and quasi-linear behavior of a curved carbon nanotube vibrating in an electric force field; an analytical approach, *Acta Mech. Solida Sin.* 27 (2014) 97–110.
- [63] M. Amjadipour, D.V. Dao, N. Motta, Vibration analysis of initially curved single walled carbon nanotube with vacancy defect for ultrahigh frequency nanoresonators, *Microsyst. Technol.* 22 (2016) 1115–1120.
- [64] H.Y. Sarvestani, H. Ghayoor, Free vibration analysis of curved nanotube structures, *Int. J. Nonlinear Mech.* 86 (2016) 167–173.
- [65] G.B. Arfken, H.J. Weber, F.E. Harris, in: G.B. Arfken, H.J. Weber, Seventh E. Harris (Eds.), Chapter 11 - Complex Variable Theory, Academic Press, Boston, 2013, pp. 469–550, <http://dx.doi.org/10.1016/B978-0-12-384654-9.00011-6>, F.E.B.T.-M.M. for P..
- [66] V.H. Weston, Toroidal wave functions, *Q. Appl. Math.* 16 (1958) 237–257, <http://www.jstor.org/stable/43634577>.
- [67] M. Andrews, Alternative separation of Laplace's equation in toroidal coordinates and its application to electrostatics, *J. Electrostat.* 64 (2006) 664–672.
- [68] H. Kraus, *Thin Elastic Shells*, John Wiley & Sons, 1967.
- [69] F. Yang, A.C.M. Chong, D.C.C. Lam, P. Tong, Couple stress based strain gradient theory for elasticity, *Int. J. Solids Struct.* 39 (2002) 2731–2743.
- [70] J.N. Reddy, J. Kim, A non-linear modified couple stress-based third-order theory of functionally graded plates, *Compos. Struct.* 94 (2012) 1128–1143, <http://dx.doi.org/10.1016/j.compstruct.2011.10.006>.
- [71] M.H. Sadd, *Elasticity: Theory, Applications, and Numerics*, Academic Press, 2009.
- [72] I. Karimpour, Y.T. Beni, H. Zeighampour, Non-linear size-dependent pull-in instability and stress analysis of ultra-thin plate actuator based on the enhanced continuum theories including surface energy effects, (n.d.).
- [73] X.H. Wang, B. Xu, D. Redekop, Theoretical natural frequencies and mode shapes for thin and thick curved pipes and toroidal shells, *J. Sound Vib.* 292 (2006) 424–434.
- [74] J. Segura, A. Gil, Evaluation of toroidal harmonics, *Comput. Phys. Comm.* 124 (2000) 104–122.
- [75] H.S. Cohl, J.E. Tohline, A.R.P. Rau, H.M. Srivastava, Developments in determining the gravitational potential using toroidal functions, *Astron. Nachr.* 321 (2000) 363–372, [http://dx.doi.org/10.1002/1521-3994\(200012\)321:5/6<363::AID-ASNA363>3.0.CO;2-X](http://dx.doi.org/10.1002/1521-3994(200012)321:5/6<363::AID-ASNA363>3.0.CO;2-X).
- [76] R.W. Scharstein, H.B. Wilson, Electrostatic excitation of a conducting toroid: exact solution and thin-wire approximation, *Electromagnetics* 25 (2005) 1–19.
- [77] Q.-M. Cheng, H. Yang, Estimates for eigenvalues on Riemannian manifolds, *J. Differential Equations* 247 (2009) 2270–2281, <http://dx.doi.org/10.1016/j.jde.2009.07.015>.
- [78] A. Gray, *Modern Differential Geometry of Curves and Surfaces with Mathematica*, first ed., CRC Press, Inc., USA, 1996.
- [79] P.M. Osterberg, S.D. Senturia, M-TEST: A test chip for MEMS material property measurement using electrostatically actuated test structures, *J. Microelectromech. Syst.* 6 (1997) 107–118, <http://dx.doi.org/10.1109/84.585788>.
- [80] Y. Cao, D.D. Nankivil, S. Allameh, W.O. Soboyejo, Mechanical properties of Au films on silicon substrates, *Mater. Manuf. Process.* 22 (2007) 187–194, <http://dx.doi.org/10.1080/10426910601062271>.
- [81] J.W. Bates, On toroidal Green's functions, *J. Math. Phys.* 38 (1997) 3679–3691, <http://dx.doi.org/10.1063/1.532061>.
- [82] C.P. Boyer, E.G. Kalnins, W. Miller, Symmetry and separation of variables for the Helmholtz and Laplace equations, *Nagoya Math. J.* (1976) <http://dx.doi.org/10.1017/S0027763000017165>.